https://doi.org/10.5194/bg-2023-39
Preprint. Discussion started: 15 March 2023

Biogeosciences
Discussions
Open Access

Characteristics of Physical and Biochemical Parameters within Mesoscale Eddies in the Southern Ocean

Qian Liu [1, 2], Yingjie Liu [1, 2], Xiaofeng Li [1, 2]

[1]CAS Key Laboratory of Ocean Circulation and Waves, Institute of Oceanology, Chinese Academy of Sciences, Qingdao 266071, China.
[2]University of Chinese Academy of Sciences, Beijing 100049, China.

Correspondence to: Yingjie Liu (yjliu@qdio.ac.cn)

Abstract. Using satellite sea surface temperature (SST) and chlorophyll-*a* (Chl-*a*) as well as observation-based reconstruction of dissolved inorganic carbon (DIC) and partial pressure of CO_2 (pCO_2) from 1996 to 2015, we analyzed the composite patterns of physical and biochemical variables over eddies in the Southern Ocean (SO). Interestingly, eddy modulation of pCO_2 has marked seasonal and regional variations. The DIC effect dominates the pCO_2 anomalies in winter. In summer, the pCO_2 anomalies within eddies are dominated by DIC (SST) anomalies in regions with larger (smaller) magnitudes of DIC anomalies. In addition, about 1/4 of eddies are observed to be abnormal (cold anticyclonic and warm cyclonic eddies) in the SO, which show opposite SST signatures contrary to normal eddies (warm anticyclonic and cold cyclonic eddies). The modification of abnormal eddies to physical and biochemical parameters is non-negligible and differs from normal eddies due to the common effects of eddy pumping and eddy-induced Ekman pumping. For example, DIC anomalies in normal and abnormal eddies show dipole patterns with opposite signals. Besides, the contributions of abnormal eddies to pCO_2 are about 2.7 times higher than normal eddies in regions where abnormal eddies dominate. However, Chl-*a* anomalies in normal and abnormal eddies show similar patterns with the same signals since they are dominated by eddy stirring and pumping.

1 Introduction

Mesoscale eddies are swirling water exiting ubiquitously in the global ocean and can influence biochemical cycling through horizontal and vertical transport water masses with physical and biochemical parameters (Altabet et al., 2012; Stramma et al., 2013; Dong et al., 2014; Song et al., 2016; Dawson et al., 2018). Eddy activity is particularly high in the Southern Ocean (SO), a critical area to global ocean dynamics (Marshall and Speer, 2012). The absorption of anthropogenic CO_2 by the SO accounts for approximately 40 % of the global ocean, and the strength of this carbon sink is variable and sensitive to changes in climate (Le Quéré et al., 2007; Landschützer et al., 2015), highlighting the tremendous importance of SO in the global climate. Therefore, it is significant to comprehensively investigate the role of eddies in regulating physical and biochemical parameters in the SO.

https://doi.org/10.5194/bg-2023-39
Preprint. Discussion started: 15 March 2023

Previous literature proposed that eddies influence physical and biochemical parameters through various mechanisms, including eddy stirring, trapping, pumping, and eddy-induced Ekman pumping (Chelton et al., 2011; Gaube et al., 2013; Dawson et al., 2018; Frenger et al., 2018). In this study, we revealed how eddies affect sea surface temperature (SST), chlorophyll-*a* (Chl-*a*), dissolved inorganic carbon (DIC), and partial pressure of CO_2 (pCO_2) through these mechanisms.

Eddy stirring and trapping are two mechanisms that redistribute physical and biochemical parameters spatially through horizontal advection. Eddy stirring refers to the local deformation of a large-scale horizontal parameter gradient via eddy rotation, resulting in dipole patterns of eddy-induced physical and biochemical parameters (Chelton et al., 2011; Frenger et al., 2015; Dawson et al., 2018; Frenger et al., 2018). For instance, under the northward increasing chlorophyll-*a* (Chl-*a*) gradient, anticyclonic eddies (AEs) would advect high Chl-*a* from the north to the southwest and low Chl-*a* from the south to the northeast. The reverse is true for cyclonic eddies (CEs). Besides, eddy trapping refers to the advective transport water masses with physical and biochemical parameters and tends to cause monopole patterns, which are determined by the directions of horizontal parameter gradient and eddy propagation (Chelton et al., 2011; Gaube et al., 2014; Mcgillicuddy, 2016). For example, under the southward increasing Chl-*a* gradient, northward/southward propagating AEs/CEs trap high/low Chl-*a*, inducing monopole positive/negative Chl-*a* anomalies.

Eddy pumping and eddy-induce Ekman pumping are the other two mechanisms that modulate and redistribute physical and biochemical parameters through vertical transports in eddy cores. Eddy pumping refers to the vertical displacement of isopycnals during the formation, growth, and destruction of mesoscale eddies (Huang et al., 2017; Dawson et al., 2018; Xu et al., 2019). Typically, AEs cause a deepening of isopycnals and downwelling with unproductive water. On the contrary, CEs lead to a doming of isopycnals and upwelling with cold, nutrient-rich deep water into the euphotic zone (Mcgillicuddy and Robinson, 1997; Mcgillicuddy et al., 1998; Nencioli et al., 2010; Lasternas et al., 2013). Therefore, eddy pumping causes negative Chl-*a* anomalies within AEs and positive Chl-*a* anomalies within CEs. However, recent studies have reported that eddy-induce Ekman pumping leads to the opposite effect with positive (negative) Chl-*a* anomalies in AEs (CEs) (Gaube et al., 2013; Gille et al., 2014; Dawson et al., 2018). Eddy-induced Ekman pumping is generated by sea surface stress curl caused by surface differential currents associated with mesoscale eddies and surface wind fields (Gaube et al., 2015). This surface stress curl has an opposite polarity to the vorticity of the eddy and thus generating Ekman upwelling (downwelling) in the cores of AEs (CEs).

Mesoscale eddies regulate SST, Chl-*a*, and DIC through these four mechanisms, affecting pCO_2 (Frenger et al., 2013; Song et al., 2016). Previous findings indicated that the pCO_2 is positively correlated with SST and DIC but negatively correlated with Chl-*a* (Chen et al., 2007; Landschützer et al., 2015; Song et al., 2016; Jersild and Ito, 2020; Iida et al., 2021). Besides, the competing seasonal cycles of SST, Chl-*a*, and DIC affect the seasonal variability of pCO_2 (Jiang et al., 2014; Munro et al., 2015; Jersild and Ito, 2020). For example, in summer, strong biological utilization of carbon causes the minimum surface DIC and pCO_2 (Takahashi et al., 2009; Munro et al., 2015; Fay et al., 2018; Jersild and Ito, 2020). On the contrary, the warm SST lowers the solubility and thus elevates pCO_2. In winter, pCO_2 increases due to the suppression of biological productivity and upwelling deep waters with high concentrations of DIC (Landschützer et al., 2015; Fay et al., 2018; Jersild and Ito, 2020). However, cold SST leads to higher solubility and thus decreases $p\mathrm{CO_2}$.

Moreover, previous studies found that the seasonal variation of $p\mathrm{CO_2}$ within the eddies varies in different regions. For example, in the Drake Passage between the Atlantic and Pacific sectors of the SO, Song et al. (2016) found that AEs/CEs have negative/positive $p\mathrm{CO_2}$ anomalies in summer, contrary to winter. They suggested that $p\mathrm{CO_2}$ within eddies is dominated by DIC (SST) in summer (winter). However, in the Georgia Basin, the Atlantic sector of the SO, Jones et al. (2017) found that both AEs and CEs have negative $p\mathrm{CO_2}$ anomalies dominated by DIC in summer. Within CEs, upwelled nutrient supply increased biological productivity, which counteracted DIC inputs from deep waters. This result is contrary to that reported by Song et al. (2016). In other regions, researchers also found different effects of eddies on $p\mathrm{CO_2}$ (Chen et al., 2007; Frenger et al., 2013). For instance, the $p\mathrm{CO_2}$ in CEs increases in the subtropical North Pacific Gyre and decreases in the SO. These findings illustrate that the mechanisms of eddy-induced modifications to $p\mathrm{CO_2}$ vary by season and region.

In addition, recent studies found that AEs can be further divided into warm and cold anticyclonic eddies (WAEs and CAEs). Similarly, CEs can be divided into cold and warm cyclonic eddies (CCEs and WCEs) depending on SST (Leyba et al., 2017; Liu et al., 2020; Liu et al., 2021; Ni et al., 2021). Consequently, WAEs and CCEs are considered normal eddies that obey conventional knowledge, and CAEs and WCEs are considered abnormal. Abnormal eddies are ubiquitous in the ocean, accounting for about 32 % of the total eddies in the global ocean, and abnormal eddies in the Antarctic Circumpolar Current (ACC) account for 19.9 % of the global total abnormal eddies (Liu et al., 2021). Moreover, the roles of abnormal eddies in ocean circulation (Shimizu et al., 2001), mass transportation (Pickart et al., 2005; Mathis et al., 2007; Everett et al., 2012), and air-sea interaction (Leyba et al., 2017; Liu et al., 2020) are different from normal ones (Assassi et al., 2016; Dilmahamod et al., 2018). For example, Pezzi et al. (2021) found a WCE causing the ocean to act locally as a $\mathrm{CO_2}$ source, contrary to the previous result that CCEs act locally as $\mathrm{CO_2}$ sinks (Chen et al., 2007; Frenger et al., 2013; Jones et al., 2017). The case study preliminarily shows the difference between normal and abnormal eddies on $p\mathrm{CO_2}$. However, how abnormal eddies in the SO affect physical and biochemical parameters remains unclear.

Previous studies of eddy-induced anomalies in the SO focused on the advective effects of eddies on Chl-*a* and did not distinguish between normal and abnormal eddies (Frenger et al., 2015; Frenger et al., 2018). However, abnormal eddies have SST anomalies opposite to normal eddies, which can potentially affect the biochemical parameters within eddies. Therefore, we aim to extend SO eddy-induced anomalies studies and examine the influence of abnormal eddies on surface physical and biochemical parameters. Using satellite SST and Chl-*a*, observation-based reconstruction of DIC and $p\mathrm{CO_2}$, and eddy datasets from 1996 to 2015, we systematically analyze their seasonal and regional variations induced by normal and abnormal eddies and examine the mechanisms driving these responses. The study is organized as follows (Fig. 1). First, Sects. 2 and 3 present data and methods. Then, in Sect. 4, we present the spatial distributions of eddy parameters, as well as spatial distributions and composite maps of eddy-induced SST, Chl-*a*, DIC, and $p\mathrm{CO_2}$ anomalies. Section 5 discusses the mechanisms driving the surface parameter's responses to eddies. Finally, we conclude in Sect. 6.

2 Data

2.1 Study region

The SO is the region between 30°S and 65°S (Fig. 2). The ACC in the SO is a global circulation that links the Pacific, Atlantic, and Indian Oceans from west to east (Marshall and Speer, 2012). We used the positions of the northern Subantarctic Front (SAF) and the Polar Front (PF) (Sallée et al., 2008) available from the Center for Topographic Studies of the Ocean and Hydrosphere (CTOH; http://ctoh.legos.obs-mip.fr/applications/mesoscale/southern-ocean-fronts). We averaged the data of the fronts over the eddy period (1996 to 2015) as boundaries for ACC major Fronts (black lines in Fig. 2).

2.2 SST, Chl-*a*, DIC, and *p*CO_2 datasets

Four datasets of sea surface parameters are used in the study, including SST, Chl-*a*, DIC, and pCO_2 from 1996 to 2015, between 30°S and 65°S. A brief description of each data is given below.

The daily SST dataset is the NOAA Optimum Interpolation (OI) SST product with 0.25° resolution, spanning from 1981 to the present (Reynolds et al., 2007). The OISST dataset combines observations from different platforms on a regular global grid, including Advanced Very High-Resolution Radiometer (AVHRR) satellite data, ships, buoys, and Argo floats with an accuracy of about 0.1 °C daily.

The Chl-*a* dataset is provided by Copernicus Marine Environmental Monitoring Service (CMEMS), based on the Copernicus-GlobColour processor that merges three algorithms (Gohin et al., 2002; Hu et al., 2012; Garnesson et al., 2019). The Chl-*a* dataset combines observations from different sensors (SeaWiFS, MODIS Aqua, MODIS Terra, MERIS, VIIRS NPP, VIIRS-JPSS1 OLCI-S3A, and S3B). The original 4 km resolution data was re-gridded to 0.25° with daily temporal resolution. We log-transform Chl-*a* using the base 10 logarithm because Chl-*a* is lognormally distributed (Campbell, 1995).

The pCO_2 and DIC datasets are from the JMA Ocean CO_2 Map dataset with monthly 1° × 1° gridded values on the global ocean from 1990 to 2020 (Iida et al., 2021). The DIC concentration is calculated from total alkalinity (TA) values and CO_2 fugacity (fCO_2) data provided by the Surface Ocean CO_2 Atlas (SOCAT), containing data from the 1950s to the present (Bakker et al., 2016). The DIC field is estimated by using a multi-linear regression (MLR) method based on the DIC and satellite observation data, including SST, sea surface salinity (SSS), sea surface dynamic height (SSDH), Chl-*a*, and surface mixed layer depth (MLD) (Iida et al., 2021).

$$\mathrm{nDIC} = f\,(\mathrm{time, SST, SSS, SSDH, Chl}\text{-}a, \mathrm{MLD})\,, \qquad (1)$$

The pCO_2 field is then calculated from TA, DIC, SST, and SSS based on seawater CO_2 chemistry. The globally averaged error in DIC was 6.1 $\mu mol\ kg^{-1}$, which is 5.4 $\mu mol\ kg^{-1}$ smaller than the error of Global Ocean Data Analysis Project version 2 update 2019 (GLODAPv2.2019), a uniformly calibrated open ocean data product on inorganic carbon and carbon-relevant variables (Olsen et al., 2019). Moreover, the error in pCO_2 was 10.9 µatm, comparable with those estimated with other empirical methods, e.g., 14.4 μatm (Landschützer et al., 2014) and 15.73 μatm (Denvil-Sommer et al., 2019). This dataset is widely used to study the relationship between $p\mathrm{CO}_2$ and physical and biochemical parameters such as biological productivity, heat, and typhoons (Yasunaka et al., 2019; Rodgers et al., 2020; Yu et al., 2020; Swierczek et al., 2021; Pittman et al., 2022)

2.3 Eddy Database

Normal and abnormal eddies were identified by a deep learning (DL) model based on the fusion of satellite sea surface height (SSH) and SST data (Liu et al., 2021). Based on the U-Net framework (Ronneberger et al., 2015; Falk et al., 2019), the model combines HyperDense-Net (Dolz et al., 2019) to fuse SSH and SST data. The SSH data is from the Archiving, Validation, and Interpretation of Satellite Oceanographic (AVISO). The SST data refers to the NOAA OISST product (Reynolds et al., 2007). The eddy data set is a daily and 0.25° resolution, including the number, radius, amplitude, rotational speed, and eddy kinetic energy (EKE) in the global ocean from 1996 to 2015. Besides, the model extracts SSH anomaly (SSHA) features for determining eddy locations and extracts SST anomaly (SSTA) information to distinguish between normal and abnormal eddies. The dice loss (a cost function to calculate the difference between the predicted and true values) and accuracy of the model was about 14 % and 94 % when training with the ground truth data set. However, due to the limitations of the resolution capability of the SSHA data (Ducet et al., 2000), eddies with amplitudes < 2 cm and radii < 35 km were discarded in this work.

3 Eddy Analysis Methodology

3.1 Eddy-centric Composite Method

To extract the eddy-induced mesoscale features in sea surface variables, including SST, Chl-*a*, DIC, and $p\mathrm{CO}_2$, we used temporal and spatial filters similar to those used in Villas Bôas et al. (2015) (Fig. 3). The temporal filter is a band-pass Butterworth window (Butterworth, 1930) applied to preserve the temporal signal between 7 and 90 days corresponding to the typical time scales of the eddies. The spatial filter is a moving average Hann window (Stearns and Ahmed, 1976) designed to contain spatial signals smaller than 600 km. This filter removes the large-scale variability unrelated to the mesoscale eddy influence. Finally, the spatial pattern of the eddy-induced anomalies in sea surface variables was estimated using composite maps. For each identified eddy with a radius of R, the eddy-induced anomalies were mapped onto the eddy-centric coordinate spanning 2R. The advantage of the eddy-centric composite method is that averaging over many eddies helps suppress noise and reveal persistent eddy structures (Melnichenko et al., 2017).

3.2 Eddy-induced Ekman pumping

At present, there are no explicit formulas to quantify eddy stirring, trapping, and pumping, but with the Ekman transport modified by the surface geostrophic vorticity ζ, the total eddy-induced Ekman pumping W_{tot} is

$$
\begin{aligned}
W_{tot} &= \frac{1}{\rho_o}\nabla \times \left[\frac{\boldsymbol{\tau}}{(f+\zeta)}\right] \\
&\approx \frac{\nabla \times \boldsymbol{\tau}}{\rho_o\,(f+\zeta)} + \frac{1}{\rho_o\,(f+\zeta)^2}\left(\tau^x\frac{\partial\zeta}{\partial y} - \tau^y\frac{\partial\zeta}{\partial x}\right),
\end{aligned}
\qquad (2)
$$

where $\rho_o = 1020$ kg m^{-3} is the (assumed constant) density of sea surface water, f is the Coriolis parameter, and the surface stress $\boldsymbol{\tau}$ has zonal and meridional components τ^x and τ^y, respectively. The surface stress curl $\nabla \times \boldsymbol{\tau}$ was computed by using finite centered differences of τ^x and τ^y. The surface geostrophic vorticity ζ is calculated as

$$
\zeta = \frac{\partial v}{\partial x} - \frac{\partial u}{\partial y}\,, \qquad (3)
$$

where u and v are the zonal and meridional components of geostrophic current velocity. The surface wind stress $\boldsymbol{\tau}$ is calculated as

$$
\boldsymbol{\tau} = \rho_a C_D (U_a - U_o)|U_a - U_o|, \qquad (4)
$$

where $\rho_a = 1.2$ kg m^{-3} is the air density (assumed constant), C_D is the drag coefficient, U_a and U_o are the wind and ocean current vectors, respectively.

U_a is a gridded Level 4 (L4) product with 0.25° resolution available every six hours from the Cross-Calibrated Multi-Platform (CCMP) ocean surface wind data set, produced by Remote Sensing Systems. The data set combines ocean surface (10m) wind retrievals from a reanalysis background field from the ERA-Interim reanalysis, multiple types of satellite microwave sensors, and observations from ships and buoys. The U_o is a daily sea surface geostrophic current product with a spatial 0.25° resolution obtained from AVISO.

To extract the mesoscale features of W_{tot}, we used temporal and spatial filters similar to those used in Gaube et al. (2015). In addition, the W_{tot} was temporally low-pass filtered with a half-power filter cutoff of 30 days and spatially high-pass filtered to contain spatial signals smaller than 600 km. Finally, we use the eddy-centric composite method to obtain the spatial pattern of eddy-induced Ekman pumping.

4 Results

4.1 Spatial Distributions of Normal and Abnormal Eddies

From 1996 to 2015, an average of 1991 eddies were identified daily in the SO (65°S–30°S), with abnormal eddies accounting for 26.3 %. Figures 4a, b, d, and e show the spatial distribution of eddy number, defined as the frequency of eddies occurrence in each 1° × 1° latitude-longitude bin over the analyzed period 1996–2015. Eddies disappear in the regions shallower than 2000m and the area near Antarctica (shown in gray in Fig. 4) because the bottom topography constrains the generation of eddies, and satellite altimetric cannot measure sea level beneath sea ice (Frenger et al., 2015). Normal and abnormal eddies are concentrated in the strong currents regions, such as the ACC, Western Boundary Current (WBC), and

Eastern Boundary Current (EBC) regions, as shown in Fig. 2. Such results are consistent with those findings by Frenger et al. (2015), which did not distinguish between normal and abnormal eddies. The differences between AEs and CEs, i.e., the eddy polarity, are critical for eddy-induced physical and biochemical anomalies (Mcgillicuddy et al., 1998; Siegel et al., 2011). Abnormal eddies have the opposite polarity distribution to normal eddies in the continental boundary currents where more CCEs and CAEs occur. The most significant difference between the polarity distributions of normal and abnormal eddies is the dominance of WCEs in southwestern Australia (SWA) (Fig. 4f).

Despite the great difference in the occurrence distributions of four kinds of eddies, their amplitude distributions are similar. The eddy amplitude is greater in the Brazil Malvinas Confluence (BMC), Agulhas Return Current (ARC), ACC, SWA, and Tasman sea (Figs. 4g, h, j, and k). One should note that the amplitudes of abnormal eddies are smaller than their normal ones (Table 1), consistent with previous studies (Liu et al., 2020; Liu et al., 2021). In addition, the spatial distributions of rotational speed and EKE correlate well with the eddy amplitude patterns (Fig. 5).

4.2 Spatial Distributions of Eddy-induced SST, Chl-*a*, DIC, and $p\mathrm{CO}_2$ Anomalies

Using the eddy-centric composite method (Fig. 3), we averaged eddy-induced SST, Chl-*a*, DIC, and $p\mathrm{CO}_2$ anomalies into 1° × 1° longitude-latitude grid boxes. The maps of the climatological imprint of eddies on SST show that the distributions of SST anomalies over normal eddies are well correlated with the amplitude distributions, with stronger positive/negative SST anomalies (in WAEs/CCEs) concentrated in the BMC, ARC, ACC, SWA, and Tasman sea (Figs. 6a, c). In contrast, in the regions with larger amplitude, CAEs/WCEs have weaker negative/positive SST anomalies (Figs. 6b, d).

Also, the distributions of Chl-*a* anomalies over both normal and abnormal eddies are similar to the amplitude distributions, with stronger negative/positive anomalies within AEs/CEs in regions of higher amplitude (Figs. 6e–h). However, in the south of the ACC, including the ACC, we found the patterns of Chl-*a* anomalies are spotty, with average positive and negative Chl-*a* anomalies in AEs and CEs, respectively. The amplitude and Chl-*a* anomalies are negatively correlated in subtropical waters north of the ACC and positively correlated along the ACC.

The distributions of DIC anomalies differ greatly from that of SST and Chl-*a* anomalies, with uniform speckles featuring average negative (positive) DIC anomalies in WAEs and WCEs (CAEs and CCEs) (Figs. 6i–l). In addition to the opposite DIC anomaly signals between normal and abnormal eddies, the DIC anomaly magnitudes of normal eddies are larger than abnormal eddies.

The patterns of eddy-induced $p\mathrm{CO}_2$ anomalies are zonal. For AEs (CEs), the $p\mathrm{CO}_2$ anomalies are positive (negative) in the north of ACC and negative (positive) along the ACC (Figs. 6m–p). However, there are some distinctions between normal and abnormal eddies. For example, in the north of ACC (including SWA) with high SST and low DIC (Figs. 7a1, b1), WAEs (WCEs) have more positive speckles compared to CAEs (CCEs). In contrast, along the ACC (including ARC) with low SST and high DIC (Figs. 7a1, b1), WAEs (WCEs) have more negative speckles compared to CAEs (CCEs).

These findings indicate variability in the spatial distribution of physical and biochemical parameters caused by normal and abnormal eddies. To further quantify the effects of eddies on different parameters, we average all eddy-centric composite maps for SST, Chl-*a*, DIC, and $p\mathrm{CO_2}$ anomalies over eddies to analyze the pattern characteristics of eddy-induced parameters. Due to seasonal variations in $p\mathrm{CO_2}$, eddies' physical and biochemical characteristics are also synthesized in summer and winter.

4.3 Composite Maps of Eddy-induced SST, Chl-*a*, DIC, $p\mathrm{CO_2}$ Anomalies

Using the eddy-centric composite method (Fig. 3), we investigated the seasonal variations of SST, Chl-*a*, DIC, and $p\mathrm{CO_2}$ associated with normal and abnormal eddies in the SO (Fig. 8). Figures 8a1–a4 and e1–e4 show the composite SST anomalies within normal and abnormal eddies in winter and summer, respectively. There are no significant differences in the signals and spatial patterns of SST anomalies within the same kind of eddies in summer and winter. Composite SST anomalies over normal eddies show asymmetric monopole patterns, with positive (negative) extremums slightly shifting westward and poleward (equatorward) relative to the WAEs (CCEs) cores. In comparison, abnormal eddies also display monopole patterns but with opposite signals. Besides, the magnitudes of SST anomalies over normal eddies are larger than abnormal eddies.

The composite Chl-*a* anomalies within the same kind of eddies also have no obvious seasonality in the signals and spatial patterns (Figs. 8b1–b4 and f1–f4). Moreover, composite Chl-*a* anomalies have no significant difference between normal and abnormal eddies, with monopole negative (positive) signals in WAEs and CAEs (CCEs and WCEs). Besides, the extremums slightly shift poleward (equatorward) relative to cores of WAEs and CAEs (CCEs and WCEs).

Regarding eddy-induced DIC anomalies, their composite maps within the same kind of eddies are similar in summer and winter, except that the magnitudes of DIC anomalies within eddies are slightly higher in winter (Figs. 8c1–c4 and g1–g4). Moreover, composite DIC anomalies within normal and abnormal eddies show dipole patterns dominated by opposite signals. WAEs (CCEs) are dominated by negative (positive) DIC anomalies, but CAEs (WCEs) are dominated by positive (negative) DIC anomalies, in contrast to SST signals.

Although $p\mathrm{CO_2}$ is influenced by SST, Chl-*a*, and DIC, $p\mathrm{CO_2}$ anomalies within eddies in winter are significantly different from summer, unlike SST, Chl-*a*, and DIC anomalies within eddies similar in summer and winter (Figs. 8d1–d4 and h1–h4). To quantify the similarity of the patterns between the $p\mathrm{CO_2}$ and other anomalies over eddies, we calculated the structural similarity index (SSIM) in Eq. (5) (Wang et al., 2004).

$$\begin{gathered} SSIM\,(X,Y) = \frac{\left(2\mu_x\mu_y + D_1\right)(2\sigma_{XY} + D_2)}{(\mu_X^2+\mu_Y^2+D_1)(\sigma_X^2+\sigma_Y^2+D_2)} \\ D_1 = (k_1L_p)^2 \\ D_2 = (k_2\mathrm{L_p})^2 \end{gathered} \tag{5}$$

where X and Y denote composite averages of normalized $p\mathrm{CO_2}$ and DIC (SST) anomalies, respectively. μ_X and μ_Y are the average values of X and Y. σ_X and σ_Y are the standard deviations of X and Y. σ_{XY} is the covariance of X and Y. L_p is the dynamic range of values, $L_p = 2$. k_1=0.01 and k_2=0.03. SSIM ranges from -1 to 1. The closer the SSIM value is to 1, the

https://doi.org/10.5194/bg-2023-39
Preprint. Discussion started: 15 March 2023

more similar the two patterns are. Because the Chl-*a* is negatively correlated with the $p\mathrm{CO}_2$, its SSIMs are multiplied by −1. In winter, the SSIMs between $p\mathrm{CO}_2$ and DIC anomalies are the largest (>0.9). The $p\mathrm{CO}_2$ anomalies have similar patterns and signals with DIC anomalies, dominant by positive signals within CAEs and CCEs and negative signals within WAEs and WCEs (Figs. 8d1–d4). However, in summer, the SSIMs are negative between $p\mathrm{CO}_2$ and DIC anomalies but positive between $p\mathrm{CO}_2$ and SST (Chl-*a*) anomalies over eddies in summer (≤ 0.35). The patterns of $p\mathrm{CO}_2$ anomalies differ from those of SST, Chl-*a*, and DIC within eddies in the SO (Figs. 8h1–h4).

5 Modulation Mechanisms of Normal and Abnormal Eddies to Physical and Biochemical Parameters

This section discusses how eddies affect SST, Chl-*a*, DIC, and $p\mathrm{CO}_2$ through various mechanisms, including eddy stirring, trapping, pumping, and eddy-induced Ekman pumping (Fig. 9).

5.1 Mechanism Analysis of Eddy's Influence on SST

Composite SST anomalies over eddies show monopole patterns, with positive (negative) in WAEs and WCEs (CCEs and CAEs) (Figs. 8a1–a4 and e1–e4). First, we analyze the effect of eddy trapping on SST, which is determined by the directions of horizontal SST gradient and eddy propagation (Frenger et al., 2015; Frenger et al., 2018). The climatology and seasonal averages of SST show that the SST is zonally distributed and decreases southward (Figs. 7a1–a3). The tracks of long-lived eddies with lifetimes longer than 1 year show that the major propagation direction of eddies is westward, with AEs propagating north and CEs propagating south (Fig. 10). Due to the southward decreasing SST, northward (southward) propagating WAEs (CCEs) would trap cold (warm) water and cause negative (positive) SST anomalies. This process contradicts the actual results, so we exclude the effect of eddy trapping on SST. Besides, the meridional and zonal phase shifts in normal eddies are proposed to be induced by the large-scale background SST gradient and eddy stirring. WAEs rotating counterclockwise through the SST gradient would advect warmer water from the north to the southeast. Conversely, CCEs rotating clockwise through the SST gradient would advect cooler water from the south to the northwest. In summary, for the advective effects of eddies, the effect of eddy trapping on SST is not reflected, and eddy stirring affects the slight shift of SST anomalies extremums within normal eddies.

For the vertical effects of eddies, eddy pumping within AEs (CEs) associated with downwelling (upwelling) induces positive (negative) SST anomalies, while eddy-induced Ekman pumping within AEs (CEs) associated with upwelling (downwelling) induces negative (positive) SST anomalies (Figs. 9c, d) (Gaube et al., 2013; Dawson et al., 2018). Such processes are consistent with the patterns of eddy-induced SST anomalies we found. Furthermore, we found that WAEs/CCEs have greater positive/negative SST anomalies in the regions with larger amplitude, while CAEs/WCEs have weaker negative/positive SST anomalies (Figs. 6a–d). This result reflects that the strength of eddy pumping is positively correlated with eddy amplitude, i.e., greater amplitude means stronger downwelling and upwelling in the cores of AEs and CEs, respectively. Table 1 shows that the amplitudes of abnormal eddies are smaller than normal eddies, which means eddy pumping of abnormal eddies is weaker than normal eddies. Hence, abnormal eddies are more likely to be influenced by eddy-induced Ekman pumping. In conclusion, within normal eddies, eddy pumping dominates the vertical heat advection, resulting in positive (negative) SST anomalies in WAEs (CCEs) (Figs. 8a1, a3, e1, and e3). However, within abnormal eddies, the effect of eddy-induced pumping overcomes the effect of eddy pumping, resulting in negative (positive) SST anomalies in CAEs (WCEs) (Figs. 8a2, a4, e2, and e4).

5.2 Mechanism Analysis of Eddy's Influence on Chl-*a*

The composite maps of eddy-induced Chl-*a* anomalies in the SO show asymmetric monopole patterns, with negative (positive) extremums shifting poleward (equatorward) relative to the AEs (CEs) cores (Figs. 8b1–b4 and f1–f4). Due to the climatological Chl-*a* increasing southward (Figs. 7b1–b3), AEs (CEs) propagating northward (southward) would trap high (low) Chl-*a*, contrary to the composite Chl-*a* anomalies over eddies. Therefore, eddy trapping has little influence on Chl-*a*. However, eddy stirring contributes to the meridional shifts of Chl-*a* anomalies in eddies. Under the southward increasing Chl-*a*, counterclockwise rotation of AEs advects low Chl-*a* from the north to the southeast and high Chl-*a* from the south to the northwest. The reverse is true for CEs. Previous works find that the dipole shapes arising from stirring tend to be asymmetric, with larger anomalies at the leading compared to the trailing side of eddies (Chelton et al., 2011; Frenger et al., 2015; Dawson et al., 2018; Frenger et al., 2018). Such patterns induced by eddy stirring are consistent with the summer composite maps of Chl-*a* anomalies (Figs. 8f1–f4) but less consistent with the winter ones (Figs. 8b1–b4), which is related to the smaller Chl-*a* gradient in winter than in summer (Figs. 7b2 and b3).

Eddy pumping induces negative (positive) Chl-*a* anomalies within AEs (CEs), while eddy-induced Ekman pumping induces positive (negative) Chl-*a* anomalies within AEs (CEs) (Dawson et al., 2018). The eddy-centric composite maps of Chl-*a* anomalies show monopole negative (positive) signals in AEs (CEs), suggesting the negligible effect of eddy-induced Ekman pumping on Chl-*a* (Figs. 8b1–b4 and f1–f4). Besides, in regions of higher amplitude, the magnitudes of eddy-induced Chl-*a* anomalies are greater (Figs. 6e–h). This result reflects the dominant effect of eddy pumping on Chl-*a* anomalies within eddies. Therefore, eddy stirring and eddy pumping are mainly responsible for the patterns of Chl-*a* anomalies within eddies in the SO.

5.3 Mechanism Analysis of Eddy's Influence on DIC

The composite DIC anomalies within normal and abnormal eddies show dipole patterns dominated by opposite signals, negative (positive) in WAEs and WCEs (CAEs and CCEs) in the SO (Figs. 8c1–c4 and g1–g4). The dipole patterns are affected by eddy stirring. For example, under the condition of southward increasing DIC (Figs. 7c1–c3), AEs (CEs) propagating northward (southward) would trap high (low) DIC. Thus, the effect of eddy trapping may contribute to the positive and negative signals of DIC anomalies within AEs and CEs, respectively. However, the advective effects of eddies cannot explain the opposite dominant signals between normal and abnormal eddies.

https://doi.org/10.5194/bg-2023-39
Preprint. Discussion started: 15 March 2023

Eddy pumping induces negative DIC anomalies within AEs through the downwelling of surface low-DIC waters and positive DIC anomalies within CEs through the upwelling of deep rich-DIC waters. The reverse is true for the effect of eddy-induced Ekman pumping on DIC anomalies. As mentioned in 5.1, the greater amplitude means stronger eddy pumping. The greater amplitude of normal eddies than abnormal eddies increases the magnitudes of negative (positive) DIC anomalies over WAEs (CCEs). Furthermore, the Ekman pumping caused by WAEs (WCEs) is stronger than that caused by CAEs (CCEs) (Figs. 11a1–a4), resulting in stronger positive (negative) DIC anomalies over WAEs (WCEs) than CAEs (CCEs). Consequently, the common effects of eddy pumping and eddy-induced Ekman pumping result in the dominant negative (positive) DIC anomalies in WAEs and WCEs (CAEs and CCEs) in the SO.

5.4 Mechanism Analysis of Eddy's Influence on *p*CO_2

In winter, the *p*CO_2 anomalies have similar patterns and signals with DIC anomalies, and the SSIMs between *p*CO_2 and DIC anomalies are the highest in the SO (Figs. 8d1–d4), suggesting that the DIC effect on *p*CO_2 is stronger than the SST and Chl-*a* effects. However, in summer, the patterns of *p*CO_2 anomalies differ significantly from the anomalies of SST, Chl-*a*, and DIC within eddies in the SO (the highest SSIMs is 0.35) (Figs. 8h1–h4). This result may be caused by different processes affecting *p*CO_2 in different regions of the SO. To prove this hypothesis, we further examined the eddy-induced SST, Chl-*a*, DIC, and *p*CO_2 anomalies in the SWA (95°–115°E, 30°–40°S) and ARC (25°–75°E, 35°–45°S), where the eddy activity is strong, and the eddy amplitude and rotation speed are high (Figs. 4, 5, magenta rectangular box), leading to strong eddy stirring, trapping and pumping (Dawson et al., 2018; Frenger et al., 2018). Moreover, we find that the eddy-induced Ekman pumping of abnormal eddies is stronger than normal eddies in the SWA, contrary to the ARC (Fig. 11).

Similar to the SO, the SSIMs between *p*CO_2 and DIC anomalies are the highest in both the SWA and ARC in winter, indicating the dominant effect of DIC on *p*CO_2 (Figs. 12d1–d4 and 13d1–d4). However, unlike the SO, the SSIMs between *p*CO_2 and SST anomalies are the highest in summer SWA (Figs. 12h1–h4). By contrast, the SSIMs between *p*CO_2 and DIC anomalies are the highest in summer ARC (Figs. 13h1–h4). These results indicate that in summer, *p*CO_2 within eddies is dominated by the SST (DIC) effect in the SWA (ARC). Under the condition of similar magnitudes of SST anomalies over eddies between the SWA and ARC, the magnitudes of DIC anomalies in the SWA are significantly less than the ARC, which may cause different processes affecting *p*CO_2 in the two regions. Likewise, the *p*CO_2 anomalies over eddies are determined by the DIC anomalies in winter, also associated with the higher magnitudes of DIC anomalies in winter than in summer. Such regional and seasonal magnitudes variation of DIC anomalies are controlled by the complex coupling of processes, biological activity (production/remineralization), vertical mixing, and air-sea gas exchanges (Racapé et al., 2010).

We further calculate the contributions of eddies to *p*CO_2 (Table 2). On average, the contributions of abnormal eddies to *p*CO_2 are smaller than normal eddies in the SO and ARC. Nevertheless, the contributions of abnormal eddies to *p*CO_2 are higher than normal eddies in the SWA. These results are related to the dominance of abnormal eddies in the SWA, caused by the stronger eddy-induced Ekman pumping of abnormal eddies, compared to the SO and ARC (Figs. 4, 11). Besides, the contributions of the ARC and SWA eddies to *p*CO_2 are higher than the SO eddies, which is caused by the regional cancellation effect in the SO (Figs. 6m–p). In the SO and ARC, the contributions of eddies to $p\mathrm{CO_2}$ in winter are higher than in summer (except WCEs in ARC), with maximum values of 2.64 % (WAEs in the SO) and 5.03 % (CCEs in the ARC). However, in the SWA, the contributions of eddies to $p\mathrm{CO_2}$ in summer are higher than in winter, with maximum values of 5.15 % in WCEs, which is about 2.7 times higher than CCE. In conclusion, the contribution of eddies to $p\mathrm{CO_2}$ varies by eddy type, region, and season.

6 Conclusions

Using the eddy-centric composite method, we investigated the effects of normal and abnormal eddies in modulating the variability of SST, Chl-*a*, DIC, and $p\mathrm{CO_2}$ in the SO from 1996 to 2015. First, we analyzed the advective effects of eddies, including eddy trapping and stirring, based on variables gradient direction and eddy migration direction. Then, based on the eddy amplitude and the calculated W_{tot}, we analyzed the vertical pumping effects of eddies, including eddy pumping and eddy-induced Ekman pumping.

For eddy-induced SST anomalies, eddy pumping contributes to the positive/negative SST anomalies in WAEs/CCEs, and eddy-induced Ekman pumping contributes to the negative/positive SST anomalies in CAEs/WCEs. Eddy stirring and eddy pumping are the main modulation processes of normal and abnormal eddies to Chl-*a* in the SO. Composite Chl-*a* anomalies display negative (positive) signatures in both WAEs and CAEs (CCEs and WCEs). Caused by eddy stirring, composite DIC anomalies show dipole patterns in both normal and abnormal eddies. Furthermore, composite DIC anomalies are dominant by negative/positive signatures in WAEs/CCEs due to eddy pumping, in contrast to that in CAEs/WCEs caused by eddy-induced Ekman pumping. There are no significant seasonal variations in eddy-induced SST, Chl-*a*, and DIC anomalies, contrary to eddy-induced $p\mathrm{CO_2}$ anomalies that vary by season and region. In winter, the $p\mathrm{CO_2}$ anomalies are negative (positive) in WAEs and WCEs (CAEs and CCEs) caused by the dominant DIC-driven effect. However, in summer, the $p\mathrm{CO_2}$ anomalies are dominated by the common effects of SST, Chl-*a*, and DIC. Moreover, the $p\mathrm{CO_2}$ anomalies within eddies are dominated by DIC (SST) anomalies in the ARC (SWA), with larger (smaller) magnitudes of DIC anomalies in summer.

The modification of abnormal eddies to physical and biochemical parameters differs from normal eddies due to the common effects of eddy pumping and eddy-induced Ekman pumping. In the SWA dominated by abnormal eddies, the contributions of abnormal eddies to $p\mathrm{CO_2}$ are opposite to normal eddies and are about twice as high as normal eddies. The current research commonly combines all the AEs or CEs and masks the presence of CAEs and WCEs with very different upper ocean properties. Given their abundance, we consider the role of abnormal eddies when investigating eddy-induced modulation in air-sea variables, which helps to estimate mesoscale eddies' impact more accurately. This work provides an observational-based study of basin-wide surface physical and biochemical parameters in the SO mesoscale eddies and will help to improve parameterizing mesoscale processes in models used to simulate and predict ocean biogeochemistry and carbon uptake.

Data availability

All data used in the analysis are available in public repositories. The OISST data is available from https://www.ncei.noaa.gov/data/sea-surface-temperature-optimum-interpolation/v2.1/access/avhrr/. The Chl-*a* product is available from https://data.marine.copernicus.eu/product/OCEANCOLOUR_GLO_BGC_L3_MY_009_103/services. The $p\mathrm{CO}_2$ and DIC datasets are available from https://www.data.jma.go.jp/gmd/kaiyou/english/co2_flux/co2_flux_data_en.html. Normal and abnormal eddies datasets are available from https://figshare.com/s/3c3b03776d9862ac85bc for peer review only. The CCMP vector wind data is available from https://www.remss.com. The AVISO altimeter current product is available from https://data.marine.copernicus.eu/product/SEALEVEL_GLO_PHY_L4_MY_008_047/services. The positions of the main ACC fronts (Polar Front and Subantarctic Front) are available from http://ctoh.legos.obs-mip.fr/data/southern-ocean-fronts-extraction-form.

Author contributions

QL, YL, and FL conceived the project. QL did the writing and original draft preparation. All authors provided feedback on the analysis and interpretation of results and contributed to reviewing and editing the manuscript. All authors have read and agreed to the published version of the manuscript.

Competing interests

The authors declare that they have no conflict of interest.

Acknowledgements

This work was supported by the Qingdao National Laboratory for Marine Science and Technology, the special fund of Shandong province (No. LSKJ202204302), the Natural Science Foundation of Shandong Province (ZR2020MD083), the National Natural Science Foundation of China (U2006211), the Strategic Priority Research Program of the Chinese Academy of Sciences (XDA19060101, and XDB42000000), Major scientific and technological innovation projects of Shandong Province (2019JZZY010102), and the CAS Program (Y9KY04101L).

References

Altabet, M. A., Ryabenko, E., Stramma, L., Wallace, D. W. R., Frank, M., Grasse, P., and Lavik, G.: An eddy-stimulated hotspot for fixed nitrogen-loss from the Peru oxygen minimum zone, Biogeosciences, 9, 4897-4908, https://doi.org/10.5194/bg-9-4897-2012, 2012.

Assassi, C., Morel, Y., Vandermeirsch, F., Chaigneau, A., Pegliasco, C., Morrow, R., Colas, F., Fleury, S., Carton, X., Klein, P., and Cambra, R.: An Index to Distinguish Surface- and Subsurface-Intensified Vortices from Surface Observations, J. Phys. Oceanogr., 46, 2529-2552, https://doi.org/10.1175/jpo-d-15-0122.1, 2016.

Bakker, D. C. E., Pfeil, B., Landa, C. S., Metzl, N., O'Brien, K. M., Olsen, A., Smith, K., Cosca, C., Harasawa, S., Jones, S. D., Nakaoka, S., Nojiri, Y., Schuster, U., Steinhoff, T., Sweeney, C., Takahashi, T., Tilbrook, B., Wada, C., Wanninkhof, R., Alin, S. R., Balestrini, C. F., Barbero, L., Bates, N. R., Bianchi, A. A., Bonou, F., Boutin, J., Bozec, Y., Burger, E. F., Cai, W. J., Castle, R. D., Chen, L., Chierici, M., Currie, K., Evans, W., Featherstone, C., Feely, R. A., Fransson, A., Goyet, C., Greenwood, N., Gregor, L., Hankin, S., Hardman-Mountford, N. J., Harlay, J., Hauck, J., Hoppema, M., Humphreys, M. P., Hunt, C. W., Huss, B., Ibánhez, J. S. P., Johannessen, T., Keeling, R., Kitidis, V., Körtzinger, A., Kozyr, A., Krasakopoulou, E., Kuwata, A., Landschützer, P., Lauvset, S. K., Lefèvre, N., Lo Monaco, C., Manke, A., Mathis, J. T., Merlivat, L., Millero, F. J., Monteiro, P. M. S., Munro, D. R., Murata, A., Newberger, T., Omar, A. M., Ono, T., Paterson, K., Pearce, D., Pierrot, D., Robbins, L. L., Saito, S., Salisbury, J., Schlitzer, R., Schneider, B., Schweitzer, R., Sieger, R., Skjelvan, I., Sullivan, K. F., Sutherland, S. C., Sutton, A. J., Tadokoro, K., Telszewski, M., Tuma, M., van Heuven, S. M. A. C., Vandemark, D., Ward, B., Watson, A. J., and Xu, S.: A multi-decade record of high-quality $f\mathrm{CO}_2$ data in version 3 of the Surface Ocean CO_2 Atlas (SOCAT), Earth Syst. Sci. Data, 8, 383-413, https://doi.org/10.5194/essd-8-383-2016, 2016.

Butterworth, S.: On the theory of filter amplifiers, Wireless Engineer 193-195, 1930.

Campbell, J. W.: The lognormal distribution as a model for bio-optical variability in the sea, J. Geophys. Res.-Oceans, 100, 13237-13254, https://doi.org/10.1029/95JC00458, 1995.

Chelton, D. B., Gaube, P., Schlax, M. G., Early, J. J., and Samelson, R. M.: The Influence of Nonlinear Mesoscale Eddies on Near-Surface Oceanic Chlorophyll, Science, 334, 328-332, https://doi.org/doi:10.1126/science.1208897, 2011.

Chen, F., Cai, W.-J., Benitez-Nelson, C., and Wang, Y.: Sea surface $p\mathrm{CO}_2$-SST relationships across a cold-core cyclonic eddy: Implications for understanding regional variability and air-sea gas exchange, Geophys. Res. Lett., 34, https://doi.org/10.1029/2006gl028058, 2007.

Dawson, H. R. S., Strutton, P. G., and Gaube, P.: The Unusual Surface Chlorophyll Signatures of Southern Ocean Eddies, J. Geophys. Res.-Oceans, 123, 6053-6069, https://doi.org/10.1029/2017JC013628, 2018.

Denvil-Sommer, A., Gehlen, M., Vrac, M., and Mejia, C.: LSCE-FFNN-v1: a two-step neural network model for the reconstruction of surface ocean $p\mathrm{CO}_2$ over the global ocean, Geosci. Model Dev., 12, 2091-2105, https://doi.org/10.5194/gmd-12-2091-2019, 2019.

Dilmahamod, A. F., Aguiar-González, B., Penven, P., Reason, C. J. C., De Ruijter, W. P. M., Malan, N., and Hermes, J. C.: SIDDIES Corridor: A Major East-West Pathway of Long-Lived Surface and Subsurface Eddies Crossing the Subtropical South Indian Ocean, J. Geophys. Res.-Oceans, 123, 5406-5425, https://doi.org/10.1029/2018JC013828, 2018.

Dolz, J., Gopinath, K., Yuan, J., Lombaert, H., Desrosiers, C., and Ben Ayed, I.: HyperDense-Net: A Hyper-Densely Connected CNN for Multi-Modal Image Segmentation, IEEE Trans. Med. Imaging, 38, 1116-1126, https://doi.org/10.1109/TMI.2018.2878669, 2019.

Dong, C. M., McWilliams, J. C., Liu, Y., and Chen, D. K.: Global heat and salt transports by eddy movement, Nat. Commun., 5, https://doi.org/10.1038/ncomms4294, 2014.

Ducet, N., Le Traon, P. Y., and Reverdin, G.: Global high-resolution mapping of ocean circulation from TOPEX/Poseidon and ERS-1 and -2, J. Geophys. Res.-Oceans, 105, 19477-19498, https://doi.org/10.1029/2000JC900063, 2000.

Everett, J. D., Baird, M. E., Oke, P. R., and Suthers, I. M.: An avenue of eddies: Quantifying the biophysical properties of mesoscale eddies in the Tasman Sea, Geophys. Res. Lett., 39, https://doi.org/10.1029/2012gl053091, 2012.

Falk, T., Mai, D., Bensch, R., Cicek, O., Abdulkadir, A., Marrakchi, Y., Bohm, A., Deubner, J., Jackel, Z., Seiwald, K., Dovzhenko, A., Tietz, O., Dal Bosco, C., Walsh, S., Saltukoglu, D., Tay, T. L., Prinz, M., Palme, K., Simons, M., Diester, I., Brox, T., and Ronneberger, O.: U-Net: deep learning for cell counting, detection, and morphometry, Nat. Methods, 16, 67-70, https://doi.org/10.1038/s41592-018-0261-2, 2019.

Fay, A. R., Lovenduski, N. S., McKinley, G. A., Munro, D. R., Sweeney, C., Gray, A. R., Landschützer, P., Stephens, B. B., Takahashi, T., and Williams, N.: Utilizing the Drake Passage Time-series to understand variability and change in subpolar Southern Ocean $p\mathrm{CO}_2$, Biogeosciences, 15, 3841-3855, https://doi.org/10.5194/bg-15-3841-2018, 2018.

Frenger, I., Münnich, M., and Gruber, N.: Imprint of Southern Ocean mesoscale eddies on chlorophyll, Biogeosciences, 15, 4781-4798, https://doi.org/10.5194/bg-15-4781-2018, 2018.

Frenger, I., Gruber, N., Knutti, R., and Münnich, M.: Imprint of Southern Ocean eddies on winds, clouds and rainfall, Nat. Geosci., 6, 608-612, https://doi.org/10.1038/ngeo1863, 2013.

Frenger, I., Münnich, M., Gruber, N., and Knutti, R.: Southern Ocean eddy phenomenology, J. Geophys. Res.-Oceans, 120, 7413-7449, https://doi.org/10.1002/2015jc011047, 2015.

Garnesson, P., Mangin, A., Fanton d'Andon, O., Demaria, J., and Bretagnon, M.: The CMEMS GlobColour chlorophyll a product based on satellite observation: multi-sensor merging and flagging strategies, Ocean Sci., 15, 819-830, https://doi.org/10.5194/os-15-819-2019, 2019.

Gaube, P., Chelton, D. B., Strutton, P. G., and Behrenfeld, M. J.: Satellite observations of chlorophyll, phytoplankton biomass, and Ekman pumping in nonlinear mesoscale eddies, J. Geophys. Res.-Oceans, 118, 6349-6370, https://doi.org/10.1002/2013JC009027, 2013.

Gaube, P., Chelton, D. B., Samelson, R. M., Schlax, M. G., and O'Neill, L. W.: Satellite Observations of Mesoscale Eddy-Induced Ekman Pumping, J. Phys. Oceanogr., 45, 104-132, https://doi.org/10.1175/jpo-d-14-0032.1, 2015.

Gaube, P., McGillicuddy Jr., D. J., Chelton, D. B., Behrenfeld, M. J., and Strutton, P. G.: Regional variations in the influence of mesoscale eddies on near-surface chlorophyll, J. Geophys. Res.-Oceans, 119, 8195-8220, https://doi.org/10.1002/2014JC010111, 2014.

Gille, S. T., Carranza, M. M., Cambra, R., and Morrow, R.: Wind-induced upwelling in the Kerguelen Plateau region, Biogeosciences, 11, 6389-6400, https://doi.org/10.5194/bg-11-6389-2014, 2014.

Gohin, F., Druon, J. N., and Lampert, L.: A five channel chlorophyll concentration algorithm applied to SeaWiFS data processed by SeaDAS in coastal waters, Int. J. Remote Sens., 23, 1639-1661, https://doi.org/10.1080/01431160110071879, 2002.

Hu, C., Lee, Z., and Franz, B.: Chlorophyll aalgorithms for oligotrophic oceans: A novel approach based on three-band reflectance difference, J. Geophys. Res.-Oceans, 117, https://doi.org/10.1029/2011JC007395, 2012.

Huang, J., Xu, F., Zhou, K., Xiu, P., and Lin, Y.: Temporal evolution of near-surface chlorophyll over cyclonic eddy lifecycles in the southeastern Pacific, J. Geophys. Res.-Oceans, 122, 6165-6179, https://doi.org/10.1002/2017JC012915, 2017.

Iida, Y., Takatani, Y., Kojima, A., and Ishii, M.: Global trends of ocean CO_2 sink and ocean acidification: an observation-based reconstruction of surface ocean inorganic carbon variables, J. Oceanogr., 77, 323-358, https://doi.org/10.1007/s10872-020-00571-5, 2021.

Jersild, A. and Ito, T.: Physical and Biological Controls of the Drake Passage pCO_2 Variability, Global Biogeochem. Cycles, 34, https://doi.org/10.1029/2020gb006644, 2020.

Jiang, C., Gille, S. T., Sprintall, J., and Sweeney, C.: Drake Passage Oceanic pCO_2: Evaluating CMIP5 Coupled Carbon–Climate Models Using in situ Observations, J. Clim., 27, 76-100, https://doi.org/10.1175/jcli-d-12-00571.1, 2014.

Jones, E. M., Hoppema, M., Strass, V., Hauck, J., Salt, L., Ossebaar, S., Klaas, C., van Heuven, S. M. A. C., Wolf-Gladrow, D., Stöven, T., and de Baar, H. J. W.: Mesoscale features create hotspots of carbon uptake in the Antarctic Circumpolar Current, Deep Sea Res. Part II, 138, 39-51, https://doi.org/10.1016/j.dsr2.2015.10.006, 2017.

Landschützer, P., Gruber, N., Bakker, D. C. E., and Schuster, U.: Recent variability of the global ocean carbon sink, Global Biogeochem. Cycles, 28, 927-949, https://doi.org/10.1002/2014gb004853, 2014.

Landschützer, P., Gruber, N., Haumann, F. A., Rödenbeck, C., Bakker, D. C. E., Heuven, S. v., Hoppema, M., Metzl, N., Sweeney, C., Takahashi, T., Tilbrook, B., and Wanninkhof, R.: The reinvigoration of the Southern Ocean carbon sink, Science, 349, 1221-1224, https://doi.org/doi:10.1126/science.aab2620, 2015.

Lasternas, S., Piedeleu, M., Sangrà, P., Duarte, C. M., and Agustí, S.: Forcing of dissolved organic carbon release by phytoplankton by anticyclonic mesoscale eddies in the subtropical NE Atlantic Ocean, Biogeosciences, 10, 2129-2143, https://doi.org/10.5194/bg-10-2129-2013, 2013.

Le Quéré, C., Rödenbeck, C., Buitenhuis, E. T., Conway, T. J., Langenfelds, R., Gomez, A., Labuschagne, C., Ramonet, M., Nakazawa, T., Metzl, N., Gillett, N., and Heimann, M.: Saturation of the Southern Ocean CO₂ Sink Due to Recent Climate Change, Science, 316, 1735-1738, https://doi.org/doi:10.1126/science.1136188, 2007.

Leyba, I. M., Saraceno, M., and Solman, S. A.: Air-sea heat fluxes associated to mesoscale eddies in the Southwestern Atlantic Ocean and their dependence on different regional conditions, Clim. Dyn., 49, 2491-2501, https://doi.org/10.1007/s00382-016-3460-5, 2017.

Liu, Y., Yu, L., and Chen, G.: Characterization of Sea Surface Temperature and Air-Sea Heat Flux Anomalies Associated With Mesoscale Eddies in the South China Sea, J. Geophys. Res.-Oceans, 125, https://doi.org/10.1029/2019jc015470, 2020.

Liu, Y., Zheng, Q., and Li, X.: Characteristics of Global Ocean Abnormal Mesoscale Eddies Derived From the Fusion of Sea Surface Height and Temperature Data by Deep Learning, Geophys. Res. Lett., 48, https://doi.org/10.1029/2021gl094772, 2021.

Marshall, J. and Speer, K.: Closure of the meridional overturning circulation through Southern Ocean upwelling, Nat. Geosci., 5, 171-180, https://doi.org/10.1038/ngeo1391, 2012.

Mathis, J. T., Pickart, R. S., Hansell, D. A., Kadko, D., and Bates, N. R.: Eddy transport of organic carbon and nutrients from the Chukchi Shelf: Impact on the upper halocline of the western Arctic Ocean, J. Geophys. Res.-Oceans, 112, https://doi.org/10.1029/2006jc003899, 2007.

McGillicuddy, D. J.: Mechanisms of Physical-Biological-Biogeochemical Interaction at the Oceanic Mesoscale, Annu. Rev. Mar. Science, 8, 125-159, https://doi.org/10.1146/annurev-marine-010814-015606, 2016.

McGillicuddy, D. J. and Robinson, A. R.: Eddy-induced nutrient supply and new production in the Sargasso Sea, Deep Sea Res. Part I, 44, 1427-1450, https://doi.org/10.1016/S0967-0637(97)00024-1, 1997.

McGillicuddy, D. J., Robinson, A. R., Siegel, D. A., Jannasch, H. W., Johnson, R., Dickey, T. D., McNeil, J., Michaels, A. F., and Knap, A. H.: Influence of mesoscale eddies on new production in the Sargasso Sea, Nature, 394, 263-266, https://doi.org/10.1038/28367, 1998.

Melnichenko, O., Amores, A., Maximenko, N., Hacker, P., and Potemra, J.: Signature of mesoscale eddies in satellite sea surface salinity data, J. Geophys. Res.-Oceans, 122, 1416-1424, https://doi.org/10.1002/2016jc012420, 2017.

Munro, D. R., Lovenduski, N. S., Stephens, B. B., Newberger, T., Arrigo, K. R., Takahashi, T., Quay, P. D., Sprintall, J., Freeman, N. M., and Sweeney, C.: Estimates of net community production in the Southern Ocean determined from time series observations (2002–2011) of nutrients, dissolved inorganic carbon, and surface ocean $p\mathrm{CO_2}$ in Drake Passage, Deep Sea Res. Part II, 114, 49-63, https://doi.org/10.1016/j.dsr2.2014.12.014, 2015.

Nencioli, F., Chang, G., Twardowski, M., and Dickey, T. D.: Optical Characterization of an Eddy-induced Diatom Bloom West of the Island of Hawaii, Biogeosciences, 7, 151-162, https://doi.org/10.5194/bg-7-151-2010, 2010.

Ni, Q., Zhai, X., Jiang, X., and Chen, D.: Abundant Cold Anticyclonic Eddies and Warm Cyclonic Eddies in the Global Ocean, J. Phys. Oceanogr., 51, 2793-2806, https://doi.org/10.1175/jpo-d-21-0010.1, 2021.

Olsen, A., Lange, N., Key, R. M., Tanhua, T., Álvarez, M., Becker, S., Bittig, H. C., Carter, B. R., Cotrim da Cunha, L., Feely, R. A., van Heuven, S., Hoppema, M., Ishii, M., Jeansson, E., Jones, S. D., Jutterström, S., Karlsen, M. K., Kozyr, A., Lauvset, S. K., Lo Monaco, C., Murata, A., Pérez, F. F., Pfeil, B., Schirnick, C., Steinfeldt, R., Suzuki, T., Telszewski, M., Tilbrook, B., Velo, A., and Wanninkhof, R.: GLODAPv2.2019 – an update of GLODAPv2, Earth Syst. Sci. Data, 11, 1437-1461, https://doi.org/10.5194/essd-11-1437-2019, 2019.

Pezzi, L. P., de Souza, R. B., Santini, M. F., Miller, A. J., Carvalho, J. T., Parise, C. K., Quadro, M. F., Rosa, E. B., Justino, F., Sutil, U. A., Cabrera, M. J., Babanin, A. V., Voermans, J., Nascimento, E. L., Alves, R. C. M., Munchow, G. B., and Rubert, J.: Oceanic eddy-induced modifications to air–sea heat and CO_2 fluxes in the Brazil-Malvinas Confluence, Sci. Rep., 11, 10648, https://doi.org/10.1038/s41598-021-89985-9, 2021.

Pickart, R. S., Weingartner, T. J., Pratt, L. J., Zimmermann, S., and Torres, D. J.: Flow of winter-transformed Pacific water into the Western Arctic, Deep Sea Res. Part II, 52, 3175-3198, https://doi.org/10.1016/j.dsr2.2005.10.009, 2005.

Pittman, N. A., Strutton, P. G., Johnson, R., Matear, R. J., and Sutton, A. J.: Relationships Between Air-Sea CO_2 Flux and New Production in the Equatorial Pacific, Global Biogeochem. Cycles, 36, e2021GB007121, https://doi.org/10.1029/2021GB007121, 2022.

Racapé, V., Monaco, L., Metzl, N., and Pierre, C.: Summer and winter distribution of ƒÂ13CDIC in surface waters of the South Indian Ocean [20°S-60°S], Tellus B: Chem. Phys. Meteorol., 62, 660-673, https://doi.org/10.1111/j.1600-0889.2010.00504.x, 2010.

Reynolds, R. W., Smith, T. M., Liu, C., Chelton, D. B., Casey, K. S., and Schlax, M. G.: Daily High-Resolution-Blended Analyses for Sea Surface Temperature, J. Clim., 20, 5473-5496, https://doi.org/10.1175/2007jcli1824.1, 2007.

Rodgers, K. B., Ishii, M., Frölicher, T. L., Schlunegger, S., Aumont, O., Toyama, K., and Slater, R. D.: Coupling of Surface Ocean Heat and Carbon Perturbations over the Subtropical Cells under Twenty-First Century Climate Change, J. Clim., 33, 10321-10338, https://doi.org/10.1175/jcli-d-19-1022.1, 2020.

Ronneberger, O., Fischer, P., and Brox, T.: U-Net: Convolutional Networks for Biomedical Image Segmentation, Medical Image Computing and Computer-Assisted Intervention – MICCAI 2015, 234-241, https://doi.org/10.48550/arXiv.1505.04597, 2015.

Sallée, J. B., Speer, K., and Morrow, R.: Response of the Antarctic Circumpolar Current to Atmospheric Variability, J. Clim., 21, 3020-3039, https://doi.org/10.1175/2007JCLI1702.1, 2008.

Siegel, D. A., Peterson, P., McGillicuddy Jr., D. J., Maritorena, S., and Nelson, N. B.: Bio-optical footprints created by mesoscale eddies in the Sargasso Sea, Geophys. Res. Lett., 38, https://doi.org/10.1029/2011GL047660, 2011.

Song, H., Marshall, J., Munro, D. R., Dutkiewicz, S., Sweeney, C., McGillicuddy, D. J., and Hausmann, U.: Mesoscale modulation of air-sea CO_2 flux in Drake Passage, J. Geophys. Res.-Oceans, 121, 6635-6649, https://doi.org/10.1002/2016jc011714, 2016.

Stearns, S. D. and Ahmed, N.: Digital Signal Analysis, IEEE Transactions on Systems, Man, and Cybernetics, SMC-6, 724-724, https://doi.org/10.1109/TSMC.1976.4309433, 1976.

Stramma, L., Bange, H. W., Czeschel, R., Lorenzo, A., and Frank, M.: On the role of mesoscale eddies for the biological productivity and biogeochemistry in the eastern tropical Pacific Ocean off Peru, Biogeosciences, 10, 7293-7306, https://doi.org/10.5194/bg-10-7293-2013, 2013.

Swierczek, S., Mazloff, M. R., Morzfeld, M., and Russell, J. L.: The Effect of Resolution on Vertical Heat and Carbon Transports in a Regional Ocean Circulation Model of the Argentine Basin, J. Geophys. Res.-Oceans, 126, e2021JC017235, https://doi.org/10.1029/2021JC017235, 2021.

Takahashi, T., Sutherland, S. C., Wanninkhof, R., Sweeney, C., Feely, R. A., Chipman, D. W., Hales, B., Friederich, G., Chavez, F., Sabine, C., Watson, A., Bakker, D. C. E., Schuster, U., Metzl, N., Yoshikawa-Inoue, H., Ishii, M., Midorikawa, T., Nojiri, Y., Körtzinger, A., Steinhoff, T., Hoppema, M., Olafsson, J., Arnarson, T. S., Tilbrook, B., Johannessen, T., Olsen, A., Bellerby, R., Wong, C. S., Delille, B., Bates, N. R., and de Baar, H. J. W.: Climatological mean and decadal change in surface ocean $p\mathrm{CO}_2$, and net sea–air CO_2 flux over the global oceans, Deep Sea Res. Part II, 56, 554-577, https://doi.org/10.1016/j.dsr2.2008.12.009, 2009.

Villas Bôas, A. B., Sato, O. T., Chaigneau, A., and Castelão, G. P.: The signature of mesoscale eddies on the air-sea turbulent heat fluxes in the South Atlantic Ocean, Geophys. Res. Lett., 42, 1856-1862, https://doi.org/10.1002/2015gl063105, 2015.

Wang, Z., Bovik, A. C., Sheikh, H. R., and Simoncelli, E. P.: Image quality assessment: from error visibility to structural similarity, IEEE Trans. Image Process., 13, 600-612, https://doi.org/10.1109/TIP.2003.819861, 2004.

Xu, G., Dong, C., Liu, Y., Gaube, P., and Yang, J.: Chlorophyll Rings around Ocean Eddies in the North Pacific, Sci. Rep., 9, 2056, https://doi.org/10.1038/s41598-018-38457-8, 2019.

Yasunaka, S., Kouketsu, S., Strutton, P. G., Sutton, A. J., Murata, A., Nakaoka, S., and Nojiri, Y.: Spatio-temporal variability of surface water $p\mathrm{CO}_2$ and nutrients in the tropical Pacific from 1981 to 2015, Deep Sea Res. Part II, 169-170, 104680, https://doi.org/10.1016/j.dsr2.2019.104680, 2019.

Yu, P., Wang, Z. A., Churchill, J., Zheng, M., Pan, J., Bai, Y., and Liang, C.: Effects of Typhoons on Surface Seawater $p\mathrm{CO}_2$ and Air-Sea CO_2 Fluxes in the Northern South China Sea, J. Geophys. Res.-Oceans, 125, e2020JC016258, https://doi.org/10.1029/2020JC016258, 2020.

Figures & tables

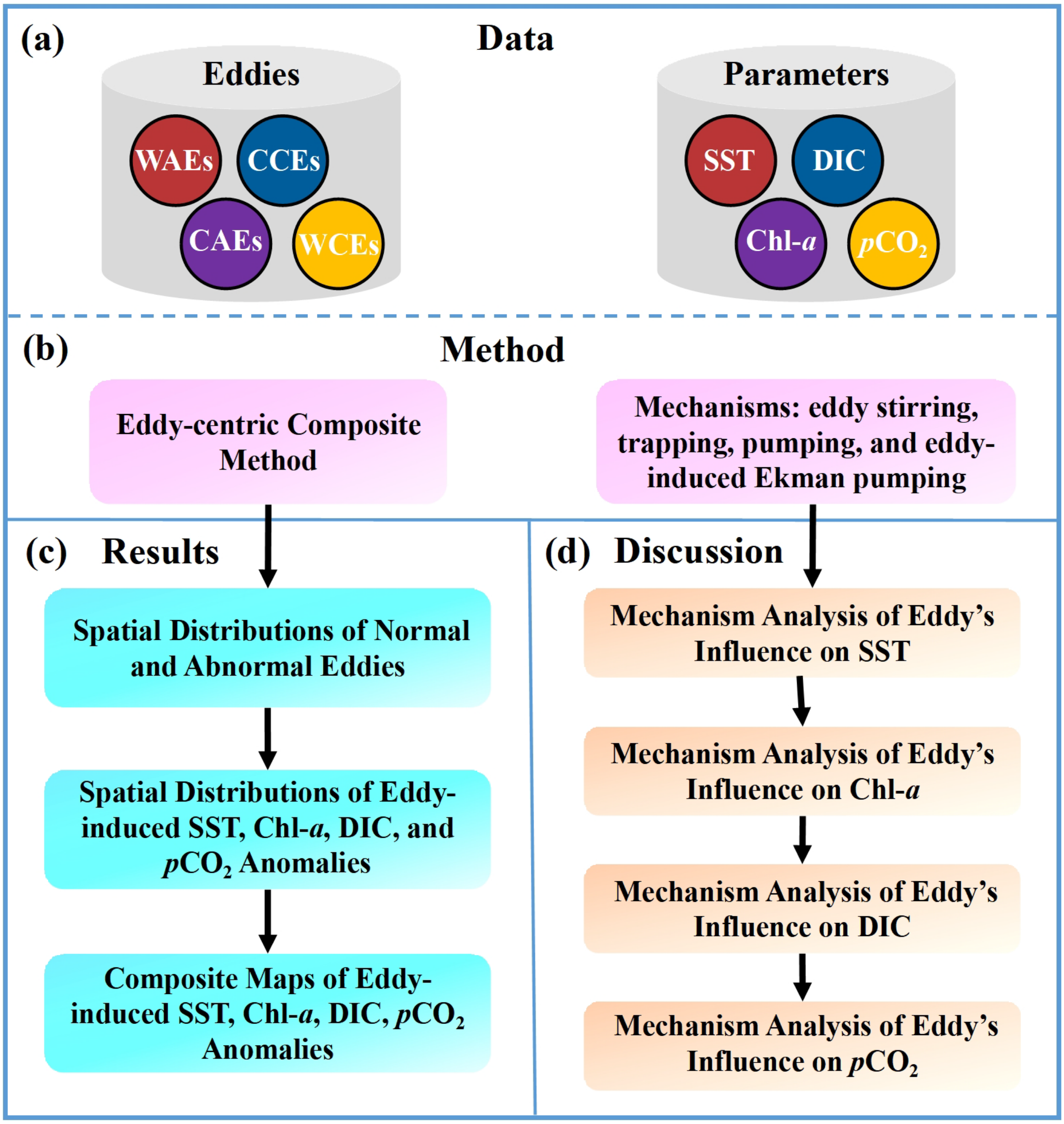

585 **Figure 1.** Research structure. Based on the eddy dataset, satellite SST and Chl-*a*, as well as observation-based reconstruction of DIC and $p\mathrm{CO}_2$ from 1996 to 2015 in the SO, we use the eddy-centric composite method to conduct the composite patterns of SST, Chl-*a*, DIC, and $p\mathrm{CO}_2$ associated with eddies. And then, we use mechanisms, including eddy stirring, trapping, pumping, and eddy-induced Ekman pumping, to analyze the modulation of eddies to SST, Chl-*a*, DIC, and $p\mathrm{CO}_2$.

https://doi.org/10.5194/bg-2023-39
Preprint. Discussion started: 15 March 2023

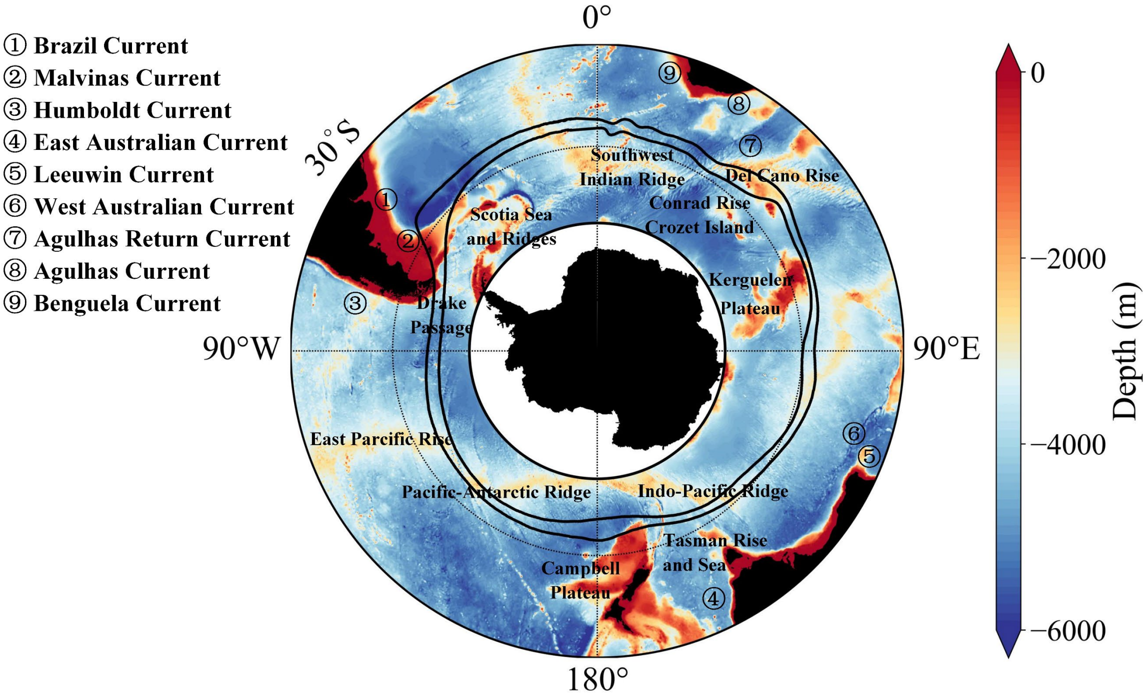

Figure 2. Southern Ocean topography and current. Black solid lines show the mean northern and southern positions of the ACC major fronts. The black dotted circle is 50° S.

https://doi.org/10.5194/bg-2023-39
Preprint. Discussion started: 15 March 2023

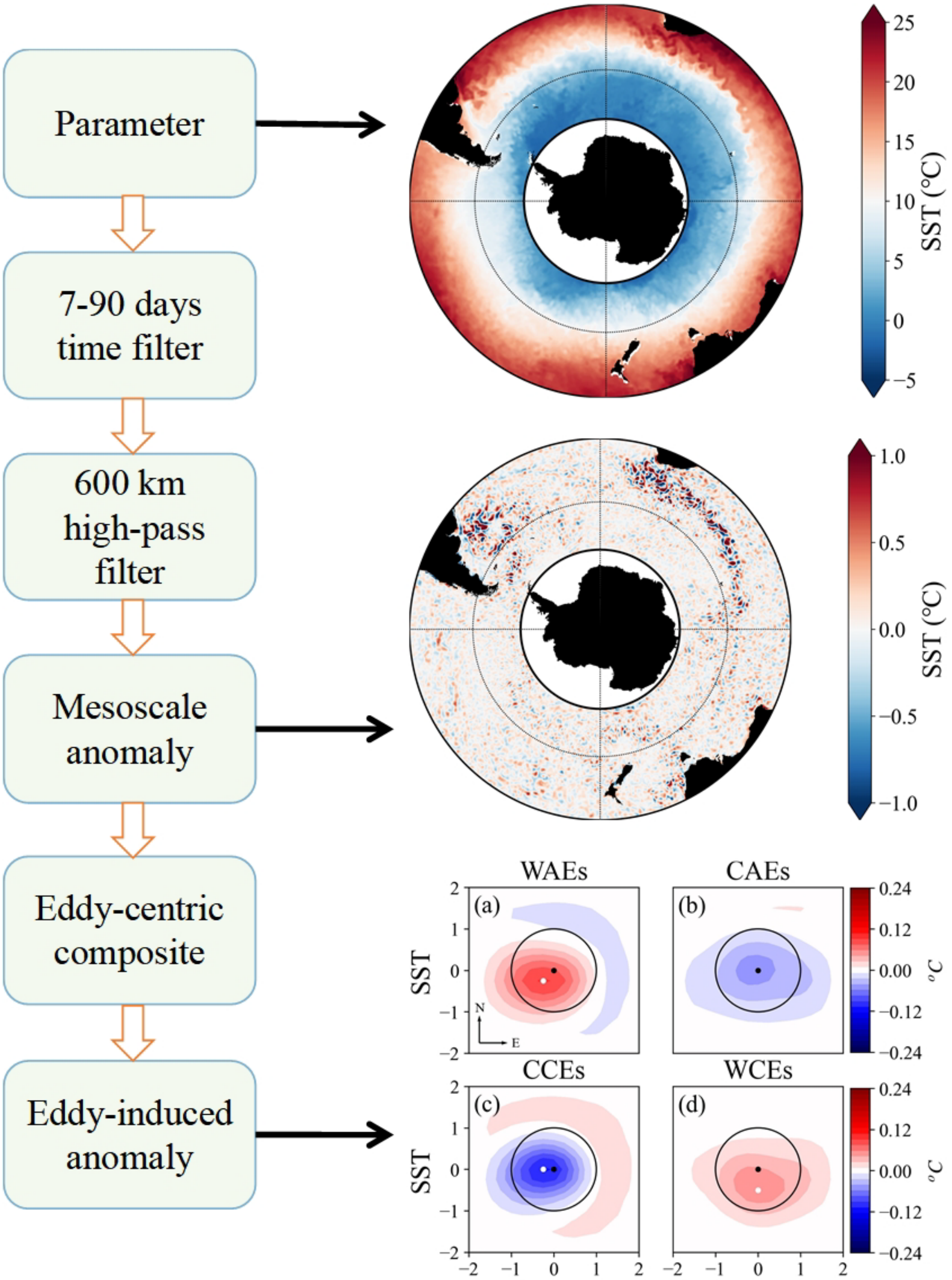

Figure 3. Schematic of eddy-centric composite method. The left column is the method structure. The right column is the result of the corresponding processing, taking SST as an example.

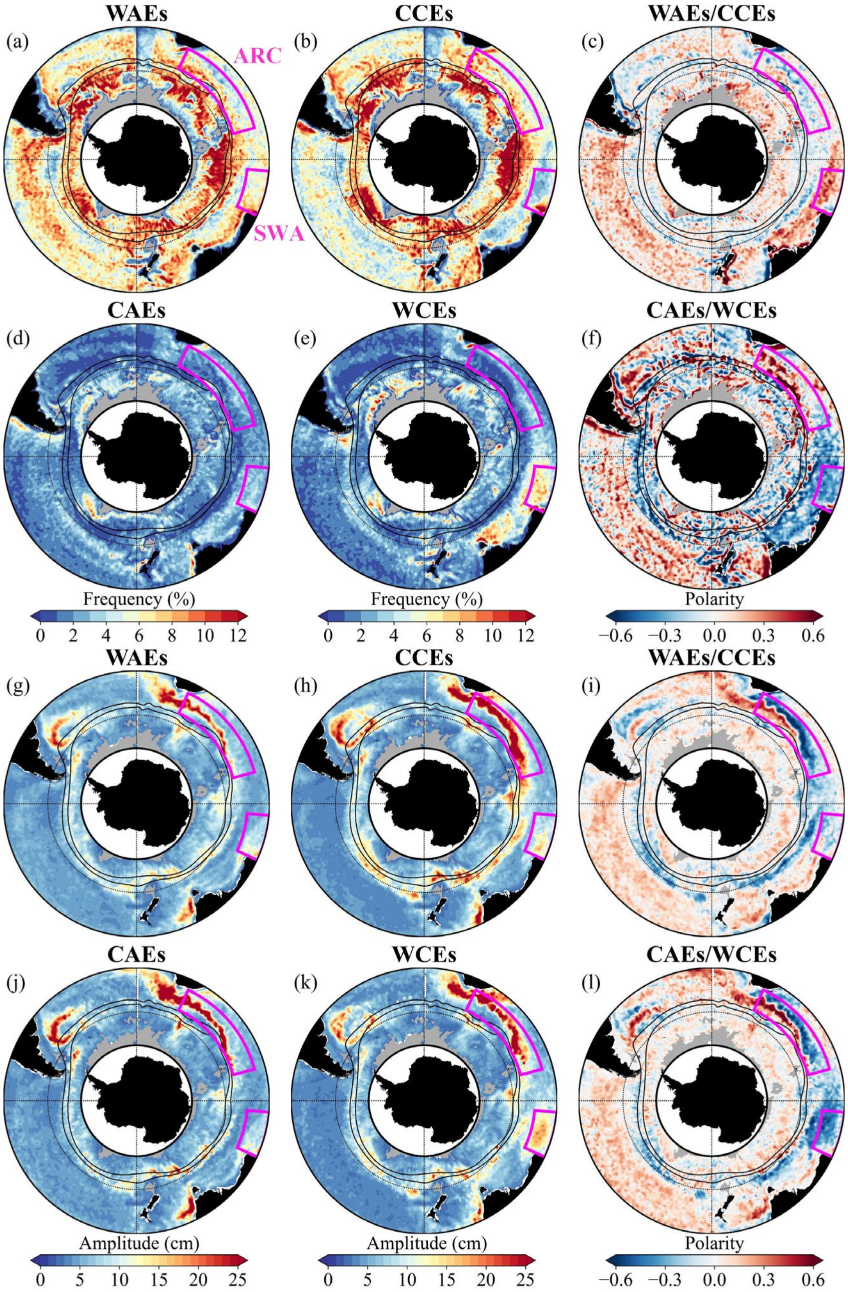

Figure 4. Spatial distribution of (a, b, d, and e) eddy frequency, (g, h, j, and k) eddy amplitude, and eddy polarity dominance in the SO from 1996 to 2015. (c, f) Ratio of the area occupied by WAEs (CAEs) over the area covered by CCEs (WCEs). (i, l) Ratio of amplitude for WAEs (CAEs) over CCEs (WCEs). Values >0 in red and <0 in blue mark the dominance of AEs and CEs, respectively. Black solid lines show the mean northern and southern positions of the ACC major fronts. The black dotted circle is 50° S.

https://doi.org/10.5194/bg-2023-39
Preprint. Discussion started: 15 March 2023

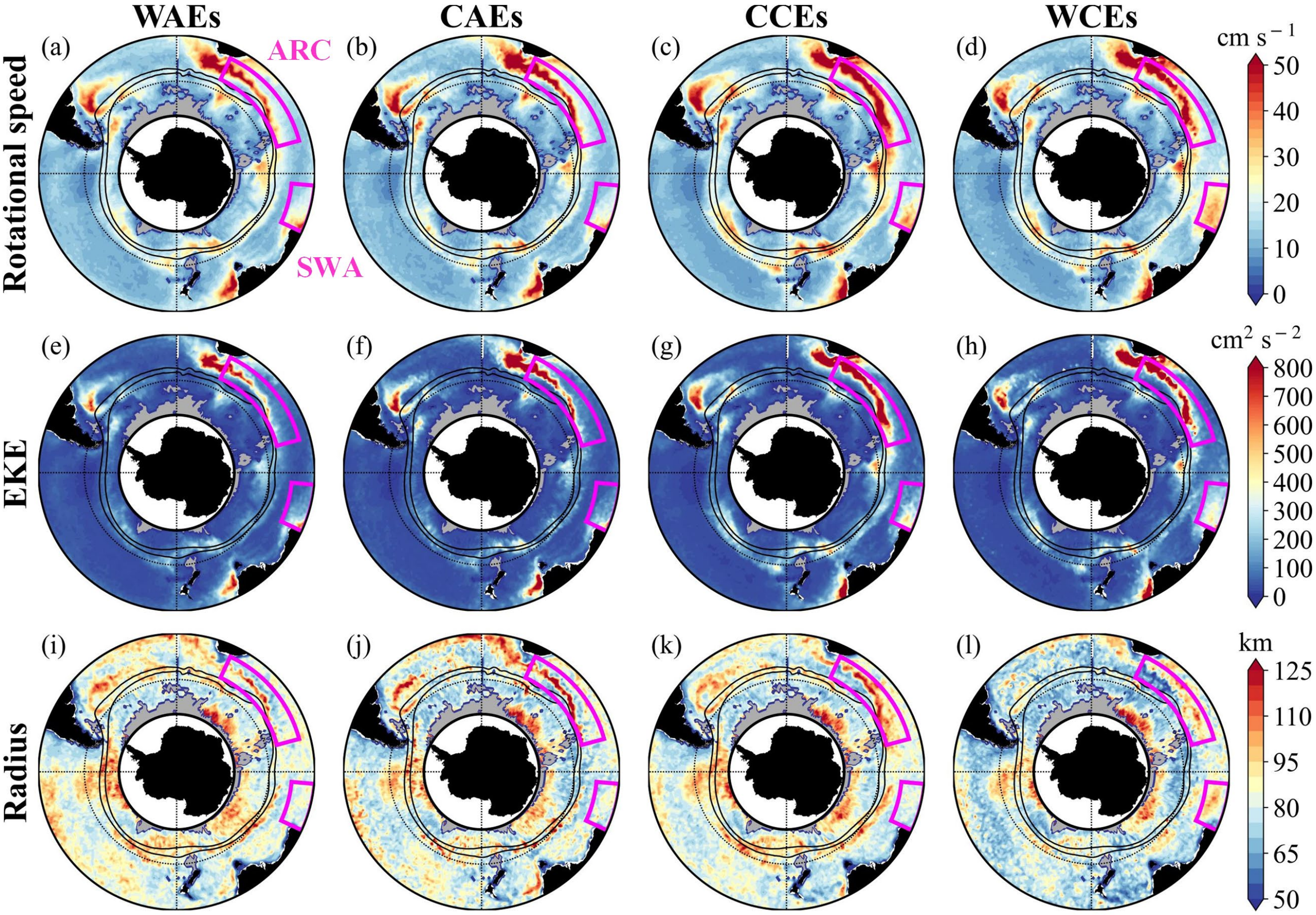

Figure 5. Spatial distribution of eddy properties, including (a–d) rotational speed, (e-h) EKE, and (i–l) radius in the Southern Ocean from 1996 to 2015. From left to right, columns represent four kinds of eddies. Black solid lines show the mean northern and southern positions of the ACC major fronts. The black dotted circle is 50° S.

https://doi.org/10.5194/bg-2023-39
Preprint. Discussion started: 15 March 2023

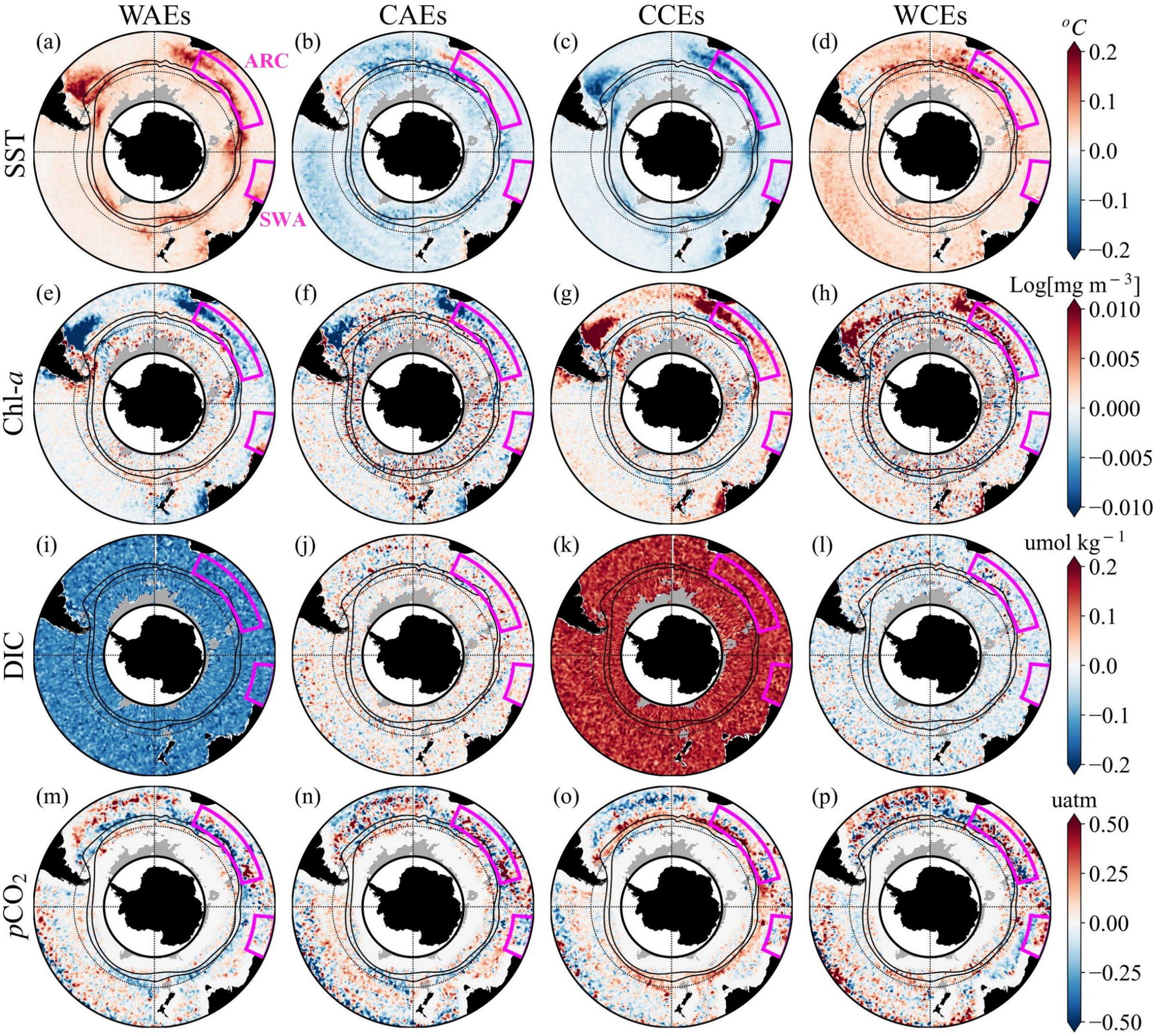

605

Figure 6. Spatial distribution of eddy-induced anomalies of (a–d) SST, (e–h) Chl-*a*, (i–l) DIC, and (m–p) $p\mathrm{CO}_2$ in the Southern Ocean from 1996 to 2015. The anomalies within eddies are averaged in 1° × 1° longitude-latitude grid boxes. From left to right, columns represent four kinds of eddies. Black solid lines show the mean northern and southern positions of the ACC major fronts. The black dotted circle is 50° S.

https://doi.org/10.5194/bg-2023-39
Preprint. Discussion started: 15 March 2023

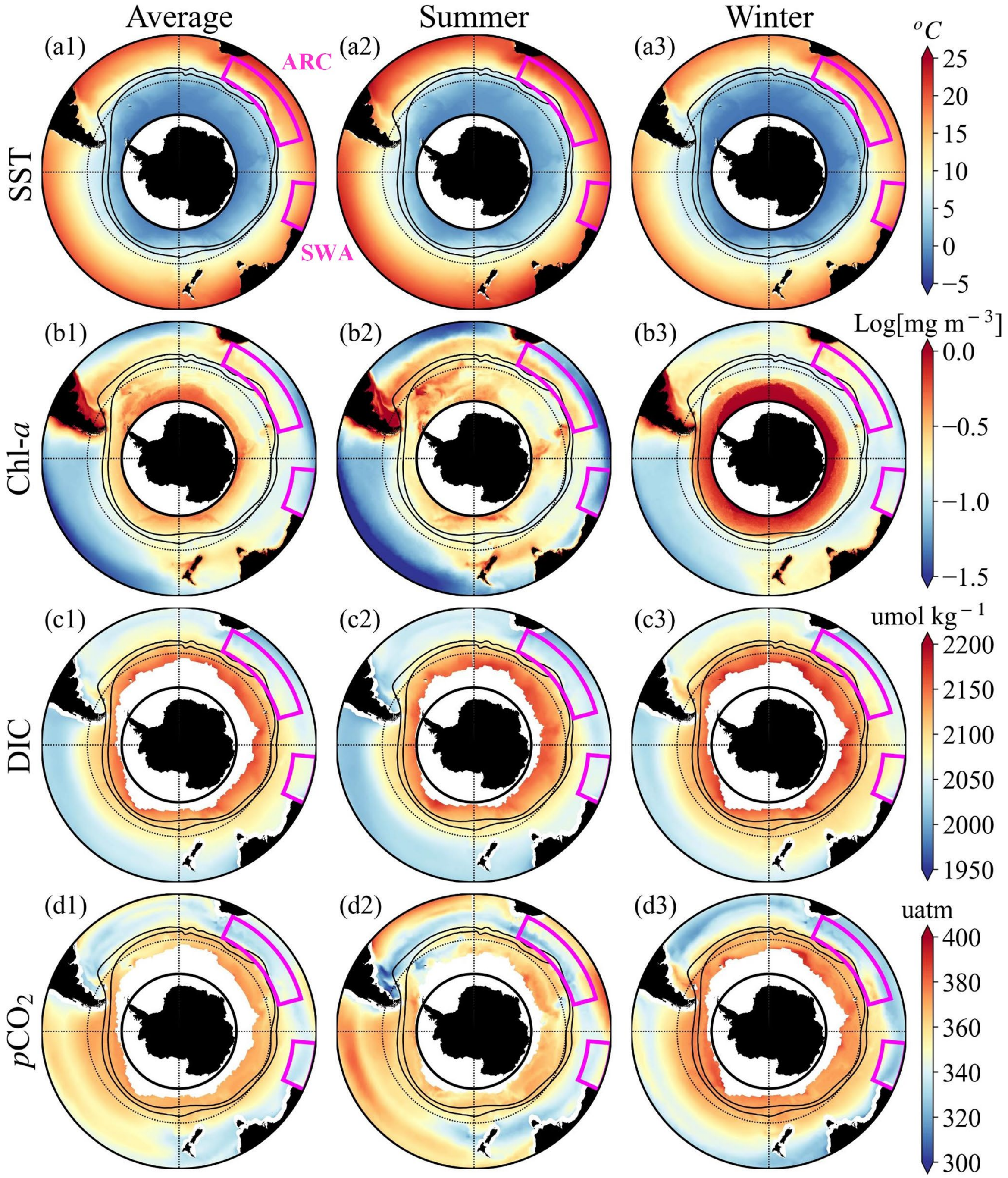

610 **Figure 7.** The climatology and seasonal averages of (a1–a3) SST, (b1–b3) Chl-*a*, (c1–c3) DIC, and (d1–d3) pCO_2 from 1996 to 2015 in the SO. Black solid lines show the mean northern and southern positions of the ACC major fronts. The black dotted circle is 50° S.

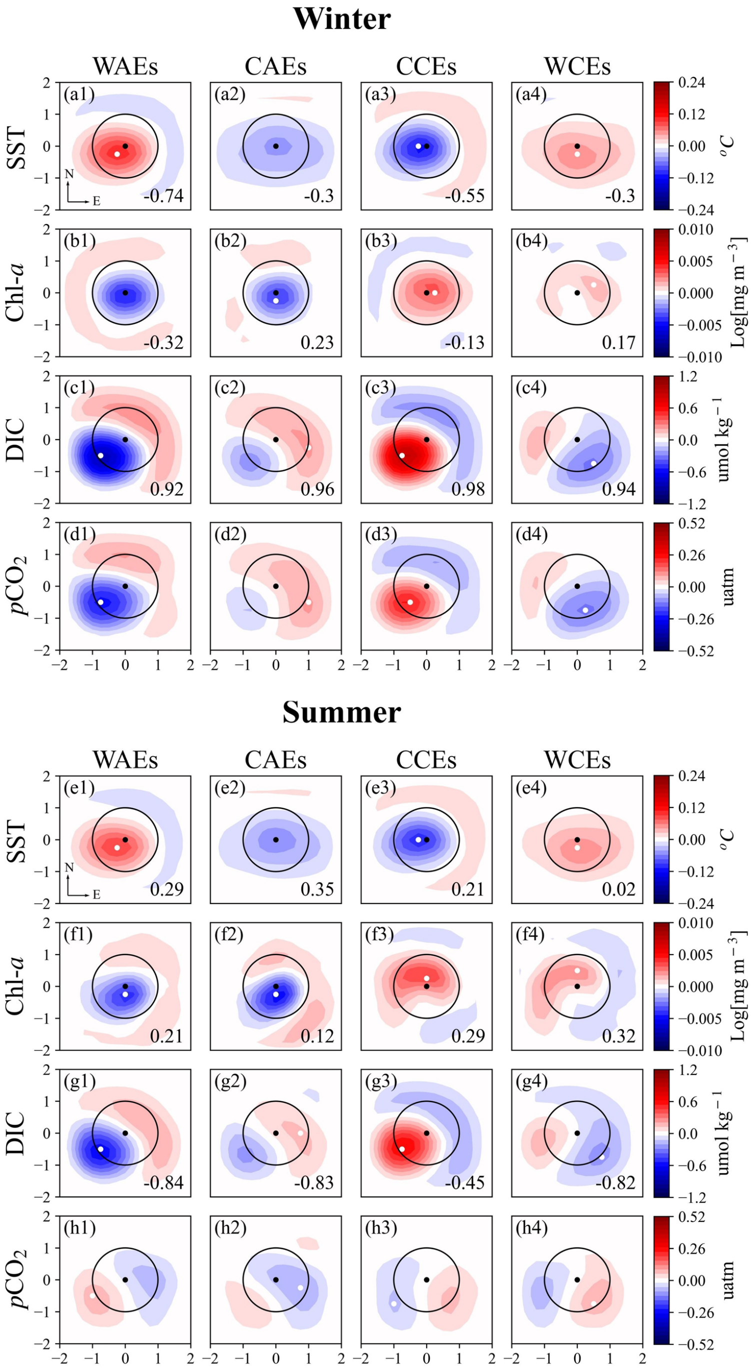

Figure 8. Eddy-centric composite averages for SST, Chl-*a*, DIC, and $p\mathrm{CO}_2$ anomalies in the SO. On each map, a black dot denotes the eddy center, and a white dot denotes the center location of variables (defined by the location of the extremum value). Contour intervals are every 0.009 °C for SST, every 0.0007 Log[mg m^{-3}] for Chl-*a*, every 0.08 umol kg^{-1} for DIC, and every 0.035 uatm for $p\mathrm{CO}_2$. The numbers in the lower right corner are the SSIMs.

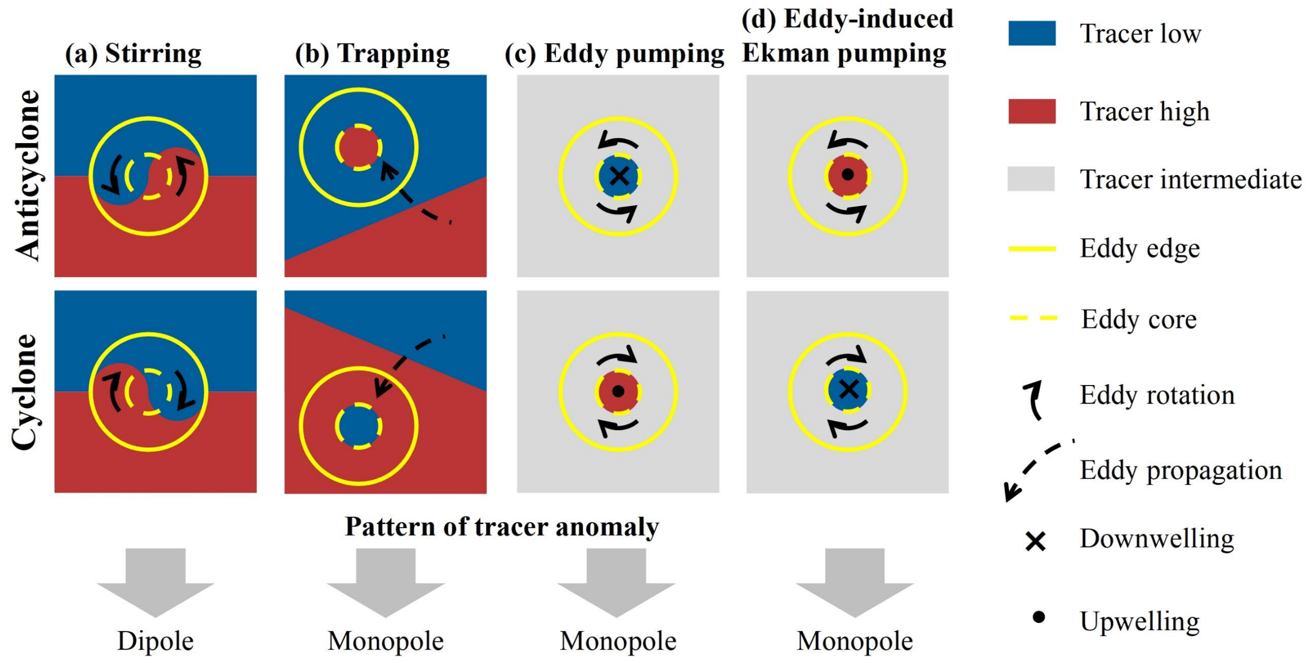

620 **Figure 9.** Schematic illustrating the mechanisms of how anticyclonic (top row) and cyclonic eddies (bottom row) affect physical and biochemical parameters in the SO, including (a) eddy stirring, (b) eddy trapping, (c) eddy pumping, and (d) eddy-induced Ekman pumping. The patterns of SST anomalies induced by vertical pumping are opposite to the corresponding patterns shown in this schematic. Figure inspired by Frenger et al. (2018), Fig. 1.

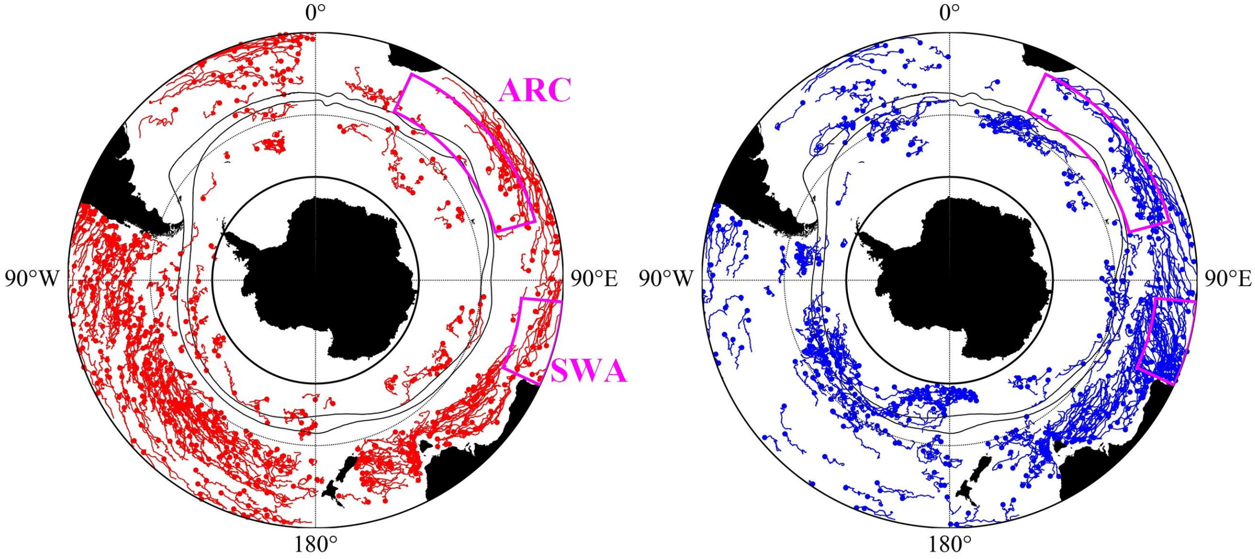

625 **Figure 10.** Trajectories of (a) AEs and (b) CEs in the SO during 1996–2015. Red (blue) dots and lines mark the AEs (CEs) birth locations and propagation paths. Only eddies with a minimum lifetime of 1 year are considered. To show the eddies tracks more clearly, only one-third of the long-lived eddies in the south and southwest of Australia have been considered. Black solid lines show the mean northern and southern positions of the ACC major fronts. The black dotted circle is 50° S.

https://doi.org/10.5194/bg-2023-39
Preprint. Discussion started: 15 March 2023

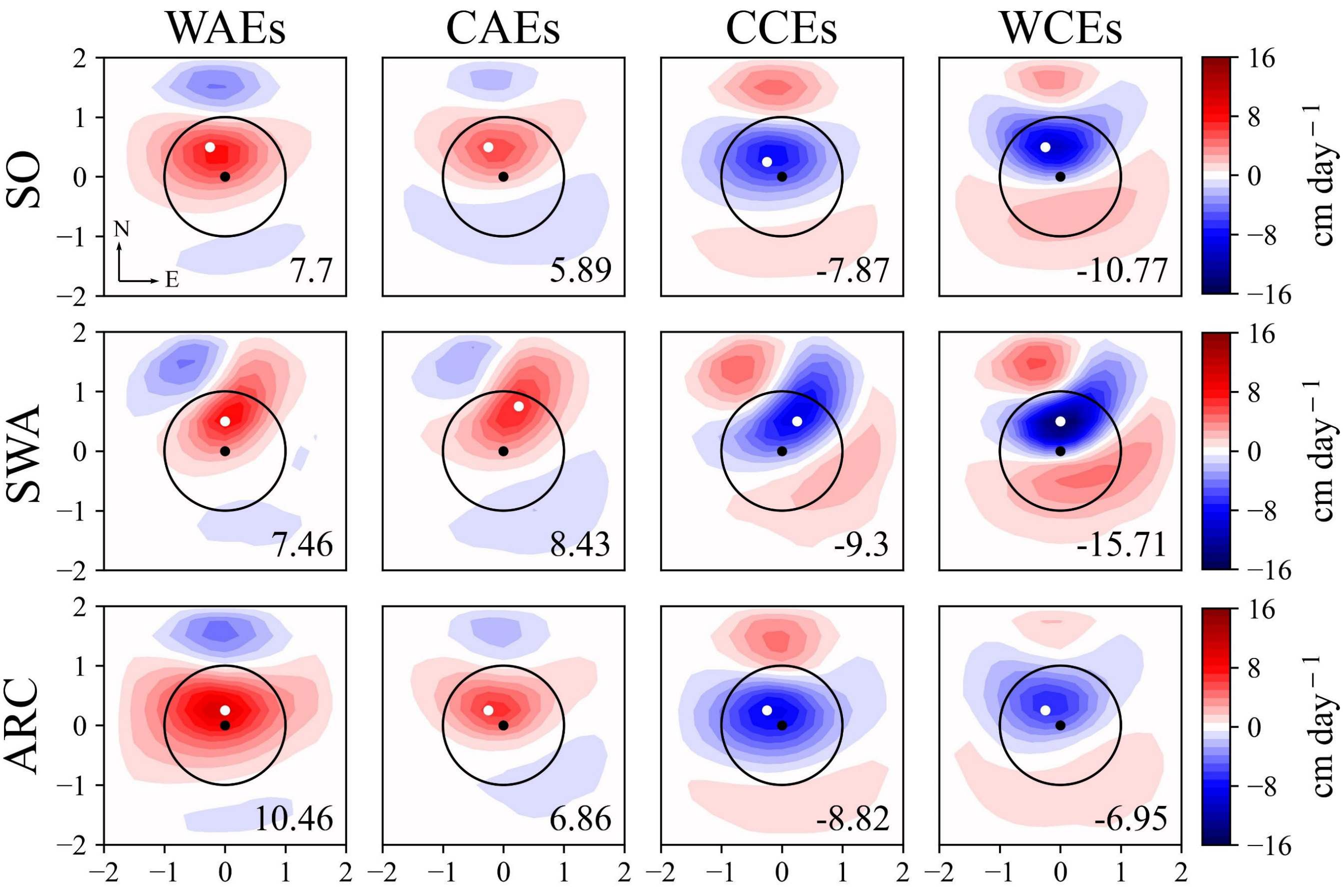

630 **Figure 11.** Eddy-centric composite averages for eddy-induced Ekman pumping in the SO, SWA, and ARC. On each map, a black dot denotes the eddy center, and a white dot denotes the center location of variables (defined by the location of the extremum value). Contour intervals are 1.067 cm day^{-1}. The numbers in the lower right corner are the extremum value.

https://doi.org/10.5194/bg-2023-39
Preprint. Discussion started: 15 March 2023

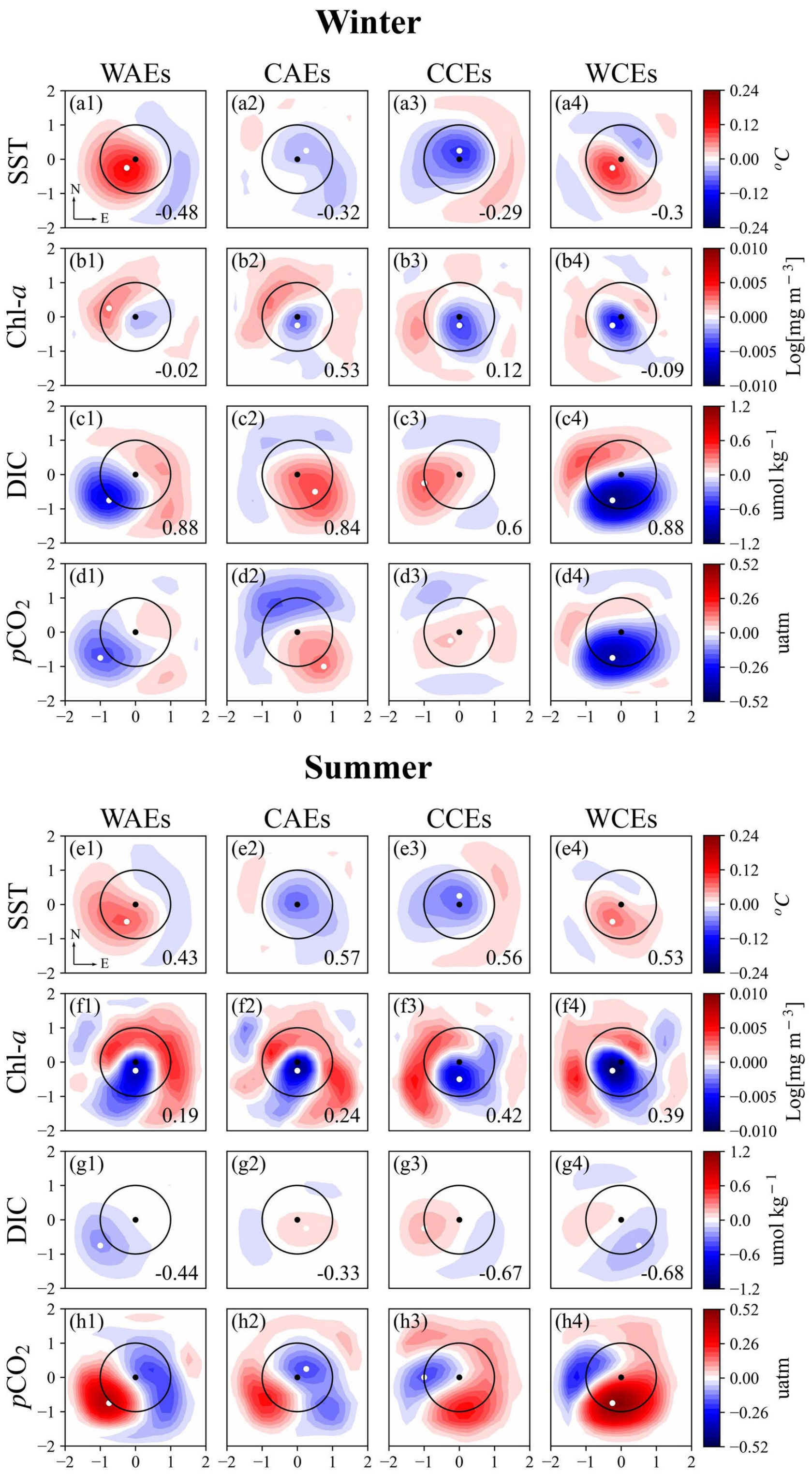

Figure 12. Same as Fig. 8 but for the SWA.

https://doi.org/10.5194/bg-2023-39
Preprint. Discussion started: 15 March 2023

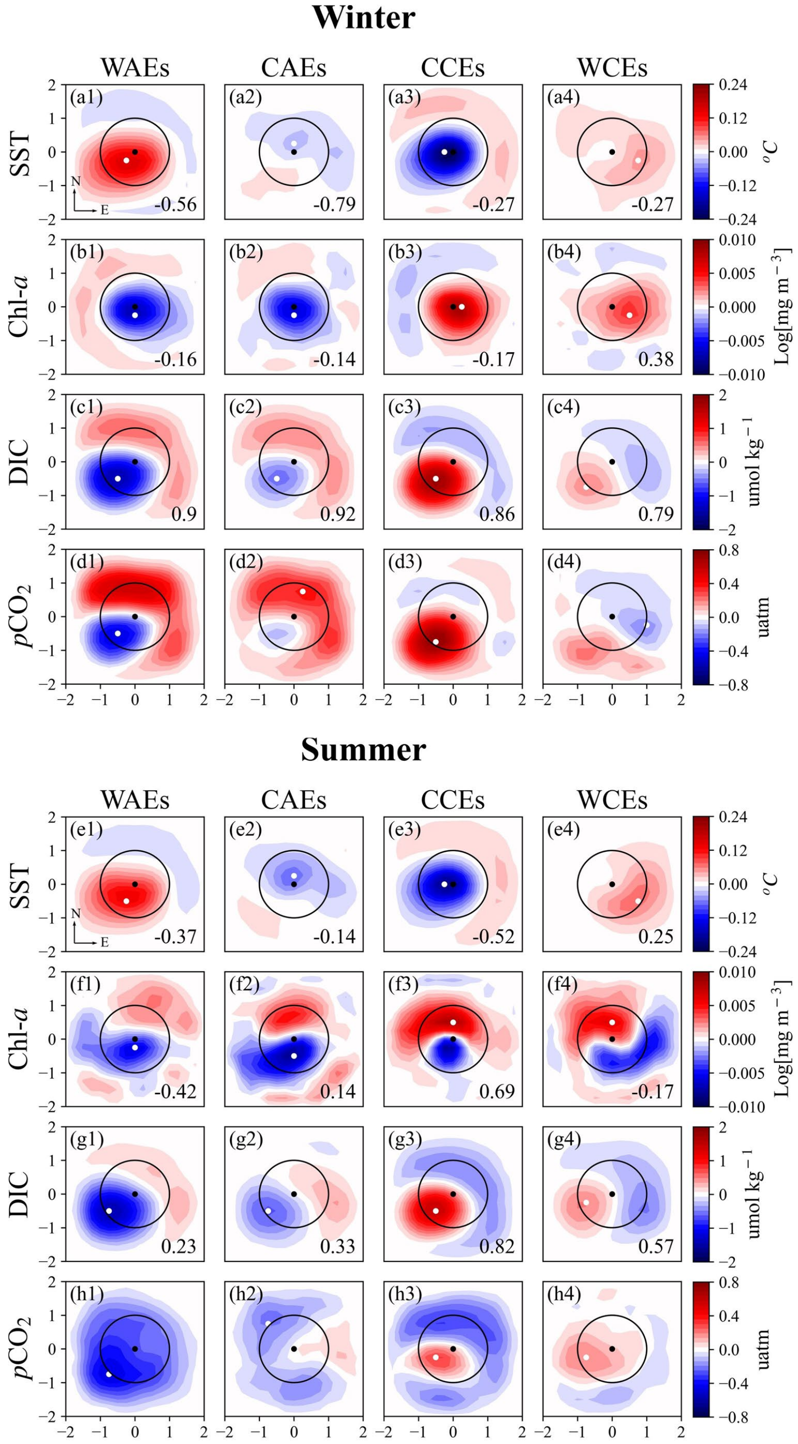

635 **Figure 13.** Same as Fig. 8 but for the ARC. And contour intervals are every 0.133 umol kg^{-1} for DIC and every 0.053 uatm for pCO$_2$.

Table 1. The climatological characteristics of mesoscale eddies in the Southern Ocean from 1996 to 2015.

	WAEs/ CAEs	CCEs/WCEs	Normal /Abnormal	AEs /CEs
Number	5450860/1786338	5261780/2043428	10712640/3829766	7237198/7305208
Amplitude (cm)	6.45/6.37	6.98/6.45	6.72/6.41	6.43/6.95
Rotational speed (cm s^{-1})	15.76/15.37	16.64/16.13	16.20/15.75	15.63/16.62
EKE (cm^2 s^{-2})	83.78/85.90	105.88/102.86	94.83/94.38	83.95/106.29
Radius (km)	88.62/87.24	87.54/82.96	88.08/85.10	88.82/87.21

https://doi.org/10.5194/bg-2023-39
Preprint. Discussion started: 15 March 2023

640 **Table 2.** Contributions of eddies to $p\mathrm{CO}_2$ in different regions and seasons from 1996 to 2015. The contributions are the percentages of the eddy-induced $p\mathrm{CO}_2$ anomalies maximum to the intra-annual variation of the corresponding variables.

Region	Eddy Type	Annual (%)	Winter (%)	Summer (%)
SO	WAEs	−0.87	−2.64	0.75
	CAEs	−0.27	1.04	−0.97
	CCEs	0.91	2.5	−0.67
	WCEs	−0.39	−1.4	0.8
SWA	WAEs	1.4	−1.76	4.12
	CAEs	−1.55	1.53	−2.06
	CCEs	−0.88	0.61	−1.91
	WCEs	1.49	−3.99	5.15
ARC	WAEs	−2.49	−3.15	−3.12
	CAEs	1.03	2.52	−1.4
	CCEs	2.53	5.03	2.06
	WCEs	−0.89	−1.19	1.26